Featured in Physics

Collective Many-Body Dynamics in a Solid-State Quantum Sensor Controlled through Nanoscale Magnetic Gradients

Piotr Put,[1,*] Nathaniel T. Leitao,[1,*] Haoyang Gao,[1,*] Christina Spaegele,[2,*] Oksana Makarova,[1,2] Lillian B. Hughes Wyatt,[3] Andrew C. Maccabe,[4] Mathew Mammen,[4] Bartholomeus Machielse,[1] Hengyun Zhou,[1] Szymon Pustelny,[1,5] Ania C. Bleszynski Jayich,[6] Federico Capasso,[2] Leigh S. Martin,[1] Hongkun Park,[1,7] and Mikhail D. Lukin[1]

[1]*Department of Physics, Harvard University, Cambridge, Massachusetts 02138, USA*
[2]*School of Engineering and Applied Sciences, Harvard University, Cambridge, Massachusetts 02138, USA*
[3]*Materials Department, University of California, Santa Barbara, California 93106, USA*
[4]*Harvard Quantum Initiative, Harvard University, Cambridge, Massachusetts 02138, USA*
[5]*Marian Smoluchowski Institute of Physics, Jagiellonian University in Kraków, 30-348 Kraków, Poland*
[6]*Department of Physics, University of California, Santa Barbara, California 93106, USA*
[7]*Department of Chemistry and Chemical Biology, Harvard University, Cambridge, Massachusetts 02138, USA*

(Received 14 October 2025; revised 10 July 2026; accepted 20 August 2026; published 16 November 2026)

Coherent collective dynamics of strongly interacting qubits are a central resource in quantum information science, with applications from quantum computing and simulation to metrology. While electronic spins interact strongly via dipolar couplings in dense solid-state ensembles, imperfections and positional disorder pose major obstacles to coherent correlated behavior, limiting their usefulness. Here, we realize collective many-body dynamics by combining time-dependent magnetic field gradients with global coherent control of dense electron spin ensembles in diamond. We control and probe the dynamics of nanometer-scale spin spirals, and, by exploiting Hamiltonian engineering that enhances the microscopic symmetry of the interactions, we observe a disorder-resilient collective spin evolution. Our results establish a pathway to interaction-enhanced quantum metrology and nanoscale imaging of materials and biological systems under ambient conditions.

DOI: 10.1103/hyrk-1ftz

Subject Areas: Atomic and Molecular Physics, Nonlinear Dynamics, Quantum Physics

I. INTRODUCTION

Coherent collective dynamics—where an isolated quantum many-body system evolves in a correlated, phase-coherent fashion—emerge either in systems composed from individually manipulated strongly coupled qubits, such as in quantum computers [1–3], or in ensembles with coherently controlled interactions [4,5]. The latter do not typically involve individual particle control, but the resulting coherent dynamics could still be useful, e.g., for reducing quantum projection noise below the standard quantum limit [6] or for amplifying weak signals amid noisy readout [7]. First proposed in the context of spectroscopy and atomic clocks [8], such dynamics have since been explored in a broad range of experimental quantum platforms, including Bose-Einstein condensates [9–11], optical-cavity-mediated atomic ensembles [12–15], and trapped ions interacting through phonons [16,17], utilizing effective all-to-all couplings mediated *indirectly* by a bosonic mode. Recently, strongly interacting systems based on *direct* dipolar spin interactions have been realized. Because of the angular averaging and sensitive position dependence of dipolar couplings, collective dynamics required the use of two-dimensional systems, such as ordered lattices of neutral atoms [5], or itinerant ultracold molecules [18,19] and neutral atoms [20]. In fact, in a three-dimensional spin ensemble, the native dipolar interaction averages to zero.

More recently, this approach has been extended to solid-state systems, which are particularly promising for realizing novel quantum sensing modalities such as nanoscale imaging in biological and material science [21–25]. While the dipolar interactions in such systems have recently been harnessed to amplify small signals [26]

[*]These authors contributed equally to this work.

Published by the American Physical Society under the terms of the Creative Commons Attribution 4.0 International license. Further distribution of this work must maintain attribution to the author(s) and the published article's title, journal citation, and DOI.

and to generate spin squeezing in subensembles of spin defects [27], their utility is severely limited by positional disorder inherent to solid-state spin ensembles [28]. In particular, naturally occurring, strongly coupled spin pairs contribute to large local energy scales that dominate the early-time dephasing, undermining the spread of collective many-body correlations [26,27].

In this article, we realize coherent, collective, many-body dynamics in a solid-state nanoscale sensor hosting positionally disordered spins in a three-dimensional ensemble. This is achieved by integrating local control through magnetic field gradients with symmetry engineering of microscopic interactions through Floquet pulse sequences. Specifically, we overcome the effects of angular averaging of the dipolar system by initializing a spatially inhomogeneous, spiral-like state with a strong magnetic field gradient and further achieve disorder-robust collective nonlinear dynamics by engineering an SU(2)-symmetric interaction that suppresses previously observed disorder-induced relaxation [26,27]. Using nanoscale imaging, we directly probe these underlying physical mechanisms, revealing collective, coherent spin exchange driving the evolution of spin spirals.

These observations extend the results of previous studies [26,27], where similar dynamics emerged at early times from native interactions in two-dimensional ensembles, while collective long-time dynamics evaded observation. Our results demonstrate a new approach for controlling such long-time many-body dynamics, in which engineering of SU(2) symmetry generates metrologically useful dynamics [6] rather than effectively decoupling interactions [29]. These observations open up opportunities for substantial metrological gain in practical, nanoscale quantum sensing.

II. CONTROLLING DENSE SPIN ENSEMBLES IN STRONG MAGNETIC GRADIENTS

Our experimental system, illustrated in Fig. 1(a), consists of a dense ensemble of nitrogen-vacancy (NV) spins in a diamond crystal [30], interacting via magnetic dipole-dipole interactions

$$H_{\mathrm{dd}} = -\sum_{i<j} \frac{\mu_0}{4\pi} \frac{(\hat{\boldsymbol{r}}_{ij}\cdot\boldsymbol{m}_i)(\hat{\boldsymbol{r}}_{ij}\cdot\boldsymbol{m}_j) - 3\boldsymbol{m}_i\cdot\boldsymbol{m}_j}{r_{ij}^3}, \quad (1)$$

where μ_0 is the magnetic permeability, $\boldsymbol{r}_{ij}$ is the interspin separation, and $\boldsymbol{m}_i$ is the quantized magnetic moment of the electronic ground state triplet. The NV electronic spins are initialized and read out using a green laser and coherently manipulated via a globally applied microwave field (Secs. VIII A and VIII B), all under ambient conditions. During the experiment, we polarize a small region within the diamond, containing between 10^3 and 10^4 spins. In this work, we use two samples: a bulk diamond plate (approximately 0.25 ppm NV density) placed on top of two parallel gold wires [Fig. 1(c)] and a denser NV sample (approximately 3.8 ppm) shaped into a triangular nanobeam (300 nm in size) and positioned atop a wire with a narrow constriction [Fig. 1(d)].

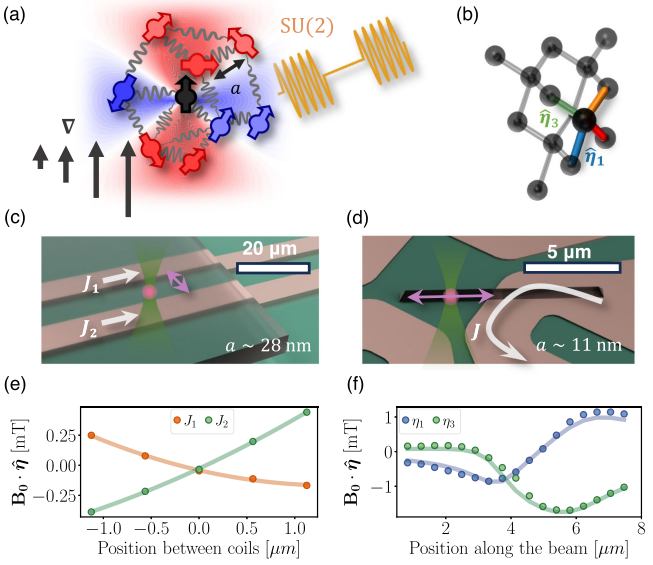


FIG. 1. Overview of the experiments. (a) Schematic illustration of the experimental system, showing a positionally disordered three-dimensional ensemble of spins interacting via anisotropic magnetic dipolar coupling (red and blue coloring) and subject to a global microwave (MW) field, which engineers SU(2) symmetric interactions between spins, and a magnetic field gradient $\boldsymbol{\nabla}$. (b) The presence of four crystallographic groups of NV centers, $\boldsymbol{\eta_\alpha}$, that also leads to different effective gradient directions $\boldsymbol{\nabla}_\alpha$. (c) Illustration of the bulk sample device, showing a diamond plate placed atop a two-wire chip that generates a magnetic field gradient tunable via the ratio of currents (J_1, J_2) on the two wires. Green laser illumination is used for spin initialization; red fluorescence indicates spin-state-dependent readout from a confocal spot. Typical spacing between spins in this sample is $a \sim 28$ nm. (d) Illustration of the nanobeam device, showing a piece of a diamond (black beam) with a dense ensemble of NV centers placed atop a microcoil that generates an inhomogeneous magnetic field $\boldsymbol{B}_0$ while running a pulsed electric current J. The sample is denser than bulk diamond, with a typical spacing between spins $a \sim 11$ nm. (e) Local magnetic field projected onto quantization axis extracted from ESR measurements for the bulk sample device, taken between microcoil wires [pink arrow in (c)] for currents running in solely each wire. Solid lines show simple quadratic fits used to determine the magnetic field gradient for this device. The plotted magnetic field projection should be understood as the average magnetic field within a 200-nm-radius region of the confocal spot. (f) ESR measurements along the nanobeam [pink arrow in (d)] for two different NV groups while running 1/10 of maximum electric current through a microcoil. Solid lines show finite-element simulations of the spatially varying magnetic field, projected onto the quantization axes of NV groups 1 and 3.

Pulsed electric currents (switchable in approximately 15 ns; see Sec. VIII F) applied to the microcoils generate a

spatially varying (inhomogeneous) magnetic field, $\boldsymbol{B}_0$ [see Fig. 1(a)], which enables local spin control and spatially resolved readout. NV centers are oriented along four different symmetry axes of the host diamond lattice [Fig. 1(b)]. A single NV group, corresponding to one of these orientations, can be selectively addressed by applying a static magnetic field aligned with its axis. This field lifts the degeneracy between different NV orientations while preserving high spin polarization and optical contrast for the selected subensemble.

At the same time, this aligned magnetic field simplifies the dipolar interactions under the secular approximation to a polarization-conserving intragroup spin-exchange interaction:

$$H_{\mathrm{dd}}^{\mathrm{eff}} = 2\sum_{i<j} J_0 \frac{A_{\hat{\boldsymbol{\eta}}}(\hat{\boldsymbol{r}}_{ij})}{r_{ij}^3}(\boldsymbol{S}_i \cdot \boldsymbol{S}_j - 2S_i^z S_j^z), \tag{2}$$

where $\boldsymbol{S}$ is the effective spin-1/2 operator defined on the qubit subspace ($m_s = 0$, $m_s = -1$) quantized along the crystallographic axis $\hat{\boldsymbol{\eta}}$ of the relevant group [31] and $J_0 = \mu_0\hbar^2\gamma^2/4\pi = \hbar \times 2\pi \times 52\ \mathrm{MHz}\cdot\mathrm{nm}^3$ sets the characteristic exchange strength via the NV gyromagnetic ratio γ and reduced Planck's constant $\hbar$. Furthermore, the spatially anisotropic coupling $A_{\hat{\boldsymbol{\eta}}}(\hat{\boldsymbol{r}}) \equiv (3(\hat{\boldsymbol{\eta}}\cdot\hat{\boldsymbol{r}})^2 - 1)/2$ can lead to either ferromagnetic or antiferromagnetic interactions depending on the orientation of the interacting spin pair relative to their mutual quantization axis $\hat{\boldsymbol{\eta}}$. Such a Hamiltonian has a U(1) symmetry generated by global rotations around the crystallographic axis and associated conservation law of total S^z polarization. The effect of the magnetic field gradient corresponding to a field profile $\boldsymbol{B}_0(\boldsymbol{r})$ is quantified by the gradient of Zeeman shift it induces. For each NV group, this corresponds to the gradient of the magnetic field projection along its quantization axis:

$$\boldsymbol{\nabla} = \nabla(\boldsymbol{B}_0 \cdot \hat{\boldsymbol{\eta}}), \tag{3}$$

where $\hat{\boldsymbol{\eta}}$ denotes a unit vector along the crystallographic symmetry axis of the relevant NV center group. The gradient direction and strength can, therefore, be continuously tuned by changing the combination of currents (J_1, J_2) running through microwires [Fig. 1(c)], affecting the magnetic field profile $\boldsymbol{B}_0(\boldsymbol{r})$. Additionally, each NV group experiences different gradient with respect to their anisotropy axis $\hat{\boldsymbol{\eta}}$ [Fig. 1(b)].

To characterize the spatial structure and strength of the gradient fields, we measure the electron spin resonance (ESR) frequency for a bulk diamond device [Fig. 1(e)] and the nanobeam [Fig. 1(f)]. We observe a clear spatial variation in the projected magnetic field $\boldsymbol{B}_0 \cdot \hat{\boldsymbol{\eta}}$, which agrees well with the predicted field profile. The resulting magnetic field gradients can reach up to approximately 2.2 mT/μm. At this gradient strength, the typical Zeeman shift difference between neighboring spins separated along the direction of $\boldsymbol{\nabla}$ exceeds their dipolar interaction by at least one order of magnitude (i.e., $\gamma|\boldsymbol{\nabla}|a \gg J_0/a^3$, with a being the typical spin-spin spacing). This enables the creation of spatially inhomogeneous spin textures within experimental coherence time and nanoscale resolution imaging required for investigating their dynamics (Sec. VIII H and Ref. [32]).

III. PROBING DYNAMICS OF NANOSCALE SPIN SPIRALS

Utilizing these strong gradient fields, we investigate dynamics of the spatially inhomogeneous spin texture with the measurement sequence illustrated in Fig. 2(a). By simultaneously controlling local magnetic gradients and global microwave pulses, the experiment is divided into three stages.

In the first stage, referred to as *winding*, spins are optically polarized along the $\hat{z}$ direction set by the crystallographic quantization axis and then globally rotated by an angle θ about the $\hat{y}$ axis using a microwave pulse as depicted in Fig. 2(b)(1). A magnetic field gradient is subsequently applied, imprinting a spatially varying Zeeman shift $\boldsymbol{\nabla}\cdot\boldsymbol{r}_j S_j^z$ across the ensemble. This phase imprinting is done in two equal duration blocks separated by a microwave π pulse to decouple local magnetic disorder, while the direction of the gradient is reversed in sync to preserve the intended local control. The resulting state is a spatially modulated spin texture, resembling a conical spin spiral [33] wound at the cone angle θ, as depicted in Fig. 2(b)(2). The magnitude of the spiral wave vector $\boldsymbol{Q} = \gamma T\boldsymbol{\nabla}$ can be controlled by adjusting the winding time T (see Sec. VIII I and Supplemental Material [34], Sec. D).

In the second stage, called *quenching*, we apply periodic microwave driving to engineer an effective many-body Hamiltonian via Floquet engineering [35]. The quench duration t is controlled by varying the number of Floquet cycles, resulting in a spin texture modified by interactions, as illustrated in Fig. 2(b)(3) together with its one-dimensional marginalization illustrated in Fig. 2(c).

In the final stage, *unwinding*, we apply an effectively reversed gradient for a variable time T', corresponding to a measurement wave vector $\boldsymbol{Q}'$. By measuring the global spin signal after this step, we effectively measure the Fourier mode $S_{\boldsymbol{Q}'}^+ = \sum_j e^{-i\boldsymbol{Q}'\cdot\boldsymbol{r}_j} S_j^+$, where $S_j^+ = S_j^x + iS_j^y$ represents the spin coherence at site j. By choosing $\boldsymbol{Q}' = \boldsymbol{Q}$, we probe the coherent dynamics of the spiral mode [Fig. 2(b)(4)].

To validate this winding-unwinding protocol on the bulk sample device [Fig. 1(c)], we prepare a spin spiral with cone angle $\theta = \pi/2$ and a pitch $Q = 2\pi/(0.242\ \mu\mathrm{m})$ and immediately reverse the process without any intermediate quench. Varying the unwinding time (and, thus, $\boldsymbol{Q}'$), we measure the ensemble-averaged x and y spin components

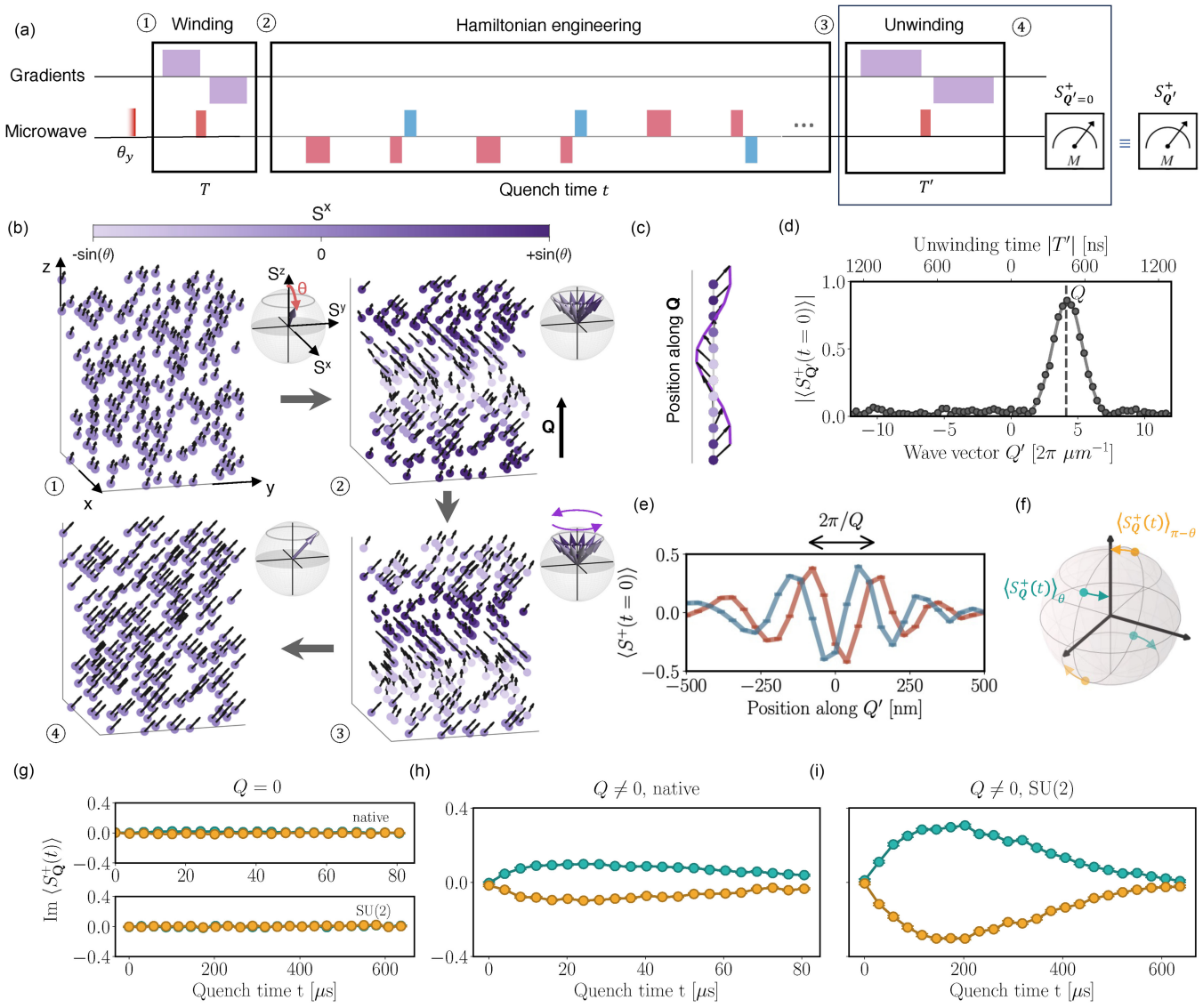


FIG. 2. Probing dynamics of conical spin spirals. (a) Schematic of the measurement protocol, consisting of three stages: spin-state preparation (winding), quench under a Floquet-engineered Hamiltonian, and readout or imaging of the spin spiral in unwinding stage. Crucial time stamps in the sequence are marked (1–4), and the corresponding spin textures are illustrated in (b). (b) Cartoon illustration of the spin texture at each step of the protocol. 1 (upper left) depicts the three-dimensional, polarized ensemble of interacting electronic spins randomly positioned within the diamond lattice. A Bloch sphere representation accompanies each texture illustration. After winding (2 and 3), the spins form a cone (gray circle connecting the tips) with position-dependent azimuthal angles, corresponding to a prepared conical spin-spiral texture. Note that the global spin measurement occurs immediately following the final step (4). Here, we neglect the effects of the π pulses during winding and unwinding steps, which is an implementation detail, since it commutes with the many-body quench and does not change the dynamics. (c) Illustration of the expected spin coherence of the conical spiral when averaged over planes perpendicular to the spiral wave vector $\boldsymbol{Q}$. (d) Benchmarking of the winding and unwinding protocol, omitting quench, demonstrating robust and reversible preparation and readout of spin spirals. Markers indicate measured points; the solid line is a simple Gaussian fit. (e) Imaging of a prepared nanoscale spin texture. Measured $\hat{x}$ (red) and $\hat{y}$ (blue) components of the spin spiral showing spin texture wound at the target pitch $\boldsymbol{Q}$. (f) Initial spin states used to probe many-body dynamics, shown on the Bloch sphere. Preparation of antipodal states (pairwise colored) enables cancellation of spurious global rotations, isolating the genuine many-body dynamics of the spin spiral [26]. (g) Measurement of many-body dynamics when no spiral is wound, reported in unit of Bloch sphere radius. The top contains data for a native dipolar interaction, while the bottom corresponds to the engineered SU(2) Hamiltonian. Without a spiral, no time-dependent signal is observed. Data are taken with the bulk sample device throughout the paper, unless explicitly stated otherwise. (h) Measurement of the spin-spiral precession dynamics for a native dipolar Hamiltonian. (i) Measurement of the spin-spiral dynamics for a Floquet engineered SU(2) Hamiltonian taken over a longer quench timescale.

[Fig. 2(d)]. We observe a clear revival in the coherence magnitude $|\langle S^+_{\boldsymbol{Q}'}(t=0)\rangle|$ centered at $Q'=Q$, providing evidence of reversible dynamics under the gradient field. The finite width of this revival profile reflects the spatial extent of the spin-polarized region [$\Delta Q' \approx 2\pi/(0.4\ \mu\text{m})$].

These data can be processed via nanoscale Fourier magnetic imaging (FMI) [24] to reconstruct spin distributions from the inverse Fourier transform of $\langle S^+_{\boldsymbol{Q}'}\rangle$. The resulting spin-spiral polarization is plotted in Fig. 2(e) and matches the expected spatial profile imposed by the wave vector $\boldsymbol{Q}$ illustrated in Fig. 2(c), confirming our ability to both prepare and measure Fourier modes of spin polarization with high fidelity.

We next proceed to investigate the many-body dynamics of spin spirals on the bulk sample device [Fig. 1(c)], focusing on the dynamics of the initialized Fourier mode $\boldsymbol{Q}'=\boldsymbol{Q}$. To isolate intrinsic many-body dynamics from accumulated microwave pulse errors, we prepare four spin spirals based on two pairs of antipodal spin-coherent states, prepared prior to winding in the XZ plane [Fig. 2(f)]. This approach allows us to average out systematic errors and spurious rotations corrupting the intrinsic nonlinearity of the many-body evolution [26].

In Figs. 2(g)–2(i), we show the extracted spiral dynamics by plotting the imaginary component of the Fourier amplitude, $\text{Im}\langle S^+_{\boldsymbol{Q}}(t)\rangle$, i.e., total $\hat{y}$ coherence measured *after* unwinding, averaged across antipodes, as a function of quench time t. When no spiral is prepared [$Q=0$, Fig. 2(g)[, no time-dependent signal is observed. For the native dipolar Hamiltonian [Eq. (2), top in Fig. 2(g)] probed via an XY-16-type decoupling sequence, this arises from angular averaging of the dipolar anisotropy, which suppresses the mean field [26,27]. A similar absence of dynamics occurs for the Floquet-engineered (Sec. VIII J), SU(2) symmetric Hamiltonian [bottom in Fig. 2(g)] which is a long-ranged, dipolar version of the quantum Heisenberg model [36]

$$H^{\text{SU(2)}}_{\text{dd}} = \sum_{i<j} \frac{\mathcal{A}_{\hat{\boldsymbol{\eta}}}(\hat{\boldsymbol{r}}_{ij})}{r^3_{ij}} \boldsymbol{S}_i \cdot \boldsymbol{S}_j, \tag{4}$$

where $\mathcal{A}_{\hat{\boldsymbol{\eta}}}(\hat{\boldsymbol{r}}) = 2J_0 A_{\hat{\boldsymbol{\eta}}}(\hat{\boldsymbol{r}})/3$ is the anisotropic coupling rescaled by average Hamiltonian engineered through a Waugh-Huber-Haeberlen sequence-type dynamical decoupling sequence [37,38]. In contrast to the native interaction, this engineered Hamiltonian has an enhanced, SU(2) symmetry generated by generic global rotations of the spin ensemble and associated conservation of *all* components of the collective spin. In this case, the total spin of the globally polarized initial state is conserved, preventing its time evolution.

In contrast, when a finite-wavelength spin spiral is initialized [$Q = 2\pi/(0.242\ \mu\text{m}) \neq 0$], we observe clear dynamical evolution of the $\hat{y}$ coherence, indicating nonlinear interaction-driven many-body dynamics [Fig. 2(h)]. The second pair of antipodal initial states exhibits similar precession dynamics but with an opposite sign. For an SU(2) symmetric Hamiltonian [Fig. 2(i)], we again observe a clear dynamical signal, similar to the one in Fig. 2(h) but on a longer timescale and with significantly higher amplitude.

IV. ENGINEERING DIPOLAR SPIN EXCHANGE

To explain the observed spin precession induced by conical spin spirals, we turn to a microscopic model where quantum spin-spin interactions are approximated by classical magnetic fields acting on each spin. We first focus on the SU(2) symmetric Hamiltonian, as the corresponding mean field has an intuitive geometric picture. As illustrated in Fig. 3(a), the mean field sourced at a central spin (black spin) is given by a (weighted) sum of the orientation of other spins through $B_{\boldsymbol{Q}} = \sum_j [\mathcal{A}_{\hat{\boldsymbol{\eta}}}(\hat{\boldsymbol{r}}_j)/r^3_j]\langle \boldsymbol{S}_j\rangle_{\boldsymbol{Q}}$, where $\langle \boldsymbol{S}_j\rangle_{\boldsymbol{Q}}$ is the polarization of the jth spin in spiral texture with wave vector $\boldsymbol{Q}$, while r_j is the distance of the jth spin to the central spin. Because of the presence of the spiral texture, this sum yields a total mean field tilted inward relative to the central spin orientation [blue arrow in Fig. 3(a)], therefore leading to its precession dynamics [cyan and orange arrows in Fig. 3(a)].

Under a conical spin spiral, the orientation of the jth spin $\langle \boldsymbol{S}_j\rangle_{\boldsymbol{Q}}$ can be expressed with the central spin orientation $\langle \boldsymbol{S}\rangle$ and the spiral wave vector $\boldsymbol{Q}$. Without loss of generality, we assume that the central spin lies in the XZ plane [Figs. 3(b) and 3(c)]. This leads to the expression of the mean field in terms of the central spin orientation (see Supplemental Material [34] Sec. G1 for derivation):

$$B_{\boldsymbol{Q}} = \left[\sum_j \frac{\mathcal{A}_{\hat{\boldsymbol{\eta}}}(\hat{\boldsymbol{r}}_j)}{r^3_j} \cos(\boldsymbol{Q}\cdot\boldsymbol{r}_j)\right]\langle S^x\rangle\hat{x} + \left[\sum_j \frac{\mathcal{A}_{\hat{\boldsymbol{\eta}}}(\hat{\boldsymbol{r}}_j)}{r^3_j}\right]\langle S^z\rangle\hat{z}, \tag{5}$$

where the first term comes from the exchange part of the interaction and the second term comes from the Ising part. The cosine factor in the first term is due to the spin texture.

There are two insightful perspectives to look at the result in Eq. (5). The first perspective is the decomposition in exchange and Ising contributions as already presented. In a 3D dipolar ensemble as in our experiment, the Ising contribution vanishes since the dipolar anisotropy [Fig. 3(d)] averages $\sum_j [\mathcal{A}_{\hat{\boldsymbol{\eta}}}(\hat{\boldsymbol{r}}_j)/r^3_j]$ to zero. Therefore, the observed spin precessions in Figs. 2(h) and 2(i) are driven by dipolar *exchange field*, in contrast to previous observation of similar phenomenon in 2D dipolar ensembles driven by Ising-like terms [26,27]. Another perspective is to further rewrite Eq. (5) to

$$B_{\boldsymbol{Q}} = -\left[\sum_j \frac{\mathcal{A}_{\hat{\boldsymbol{\eta}}}(\hat{\boldsymbol{r}}_j)}{r^3_j}(1-\cos(\boldsymbol{Q}\cdot\boldsymbol{r}_j))\right]\langle S^x\rangle\hat{x} + \left[\sum_j \frac{\mathcal{A}_{\hat{\boldsymbol{\eta}}}(\hat{\boldsymbol{r}}_j)}{r^3_j}\right]\langle \boldsymbol{S}\rangle, \tag{6}$$

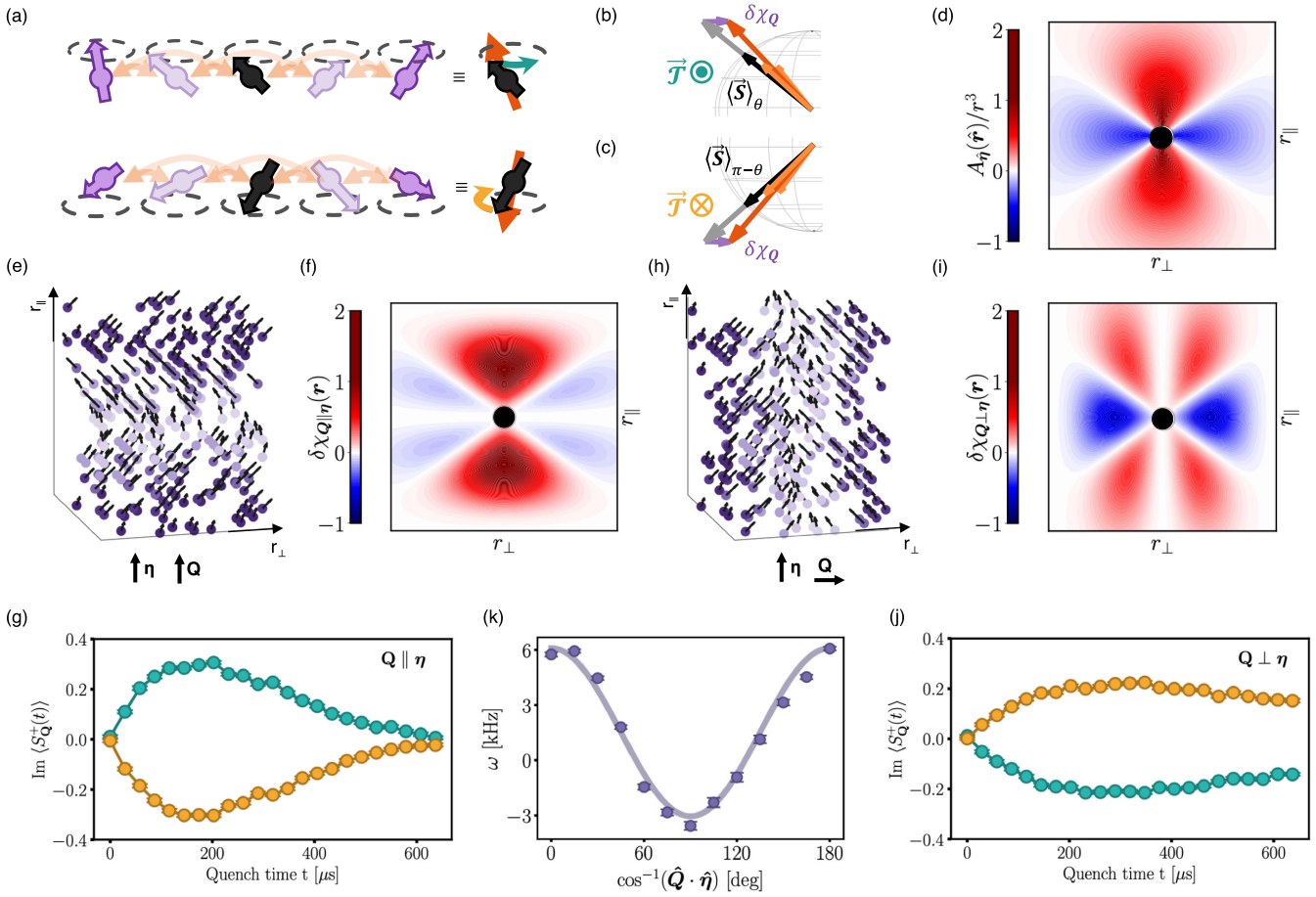


FIG. 3. Tuning dipolar spin dynamics via geometric anisotropy. (a) Semiclassical mechanism generating spiral precession due to exchange mean fields for SU(2) Hamiltonian. The central spin (black arrow) experiences an effective mean field (dark orange arrow) from nearby spins in the spiral (gray arrows). The exchange interaction is illustrated through orange arrows connecting spins. The transverse components of this field lead to spin precession (cyan arrow). Bottom: for a spiral starting from an initial state on the lower hemisphere of the Bloch sphere, the direction of the mean field and the sign of the precession are reversed (orange arrow). (b) Illustration of the exchange field sourced at a central spin (black arrow) for the spiral prepared in a state in the upper Bloch hemisphere $[\theta \in [0, \pi/2)]$. Orange arrows correspond to the field contributions from two neighbors along $\boldsymbol{Q}$, separated by equal and opposite distances. The resulting field (dark orange arrow) has a component ($\delta\chi_{\boldsymbol{Q}}$) not aligned to the central spin direction $\langle\vec{\boldsymbol{S}}\rangle_\theta$, producing a torque $\boldsymbol{\mathcal{T}}$ that leads to precession. (c) Illustration of the exchange field sourced by a central spin (black arrow) for the spiral prepared in a state in the lower Bloch hemisphere. Note that the torque $\boldsymbol{\mathcal{T}}$ on the central spin has a reversed direction compared to (b), leading to an opposite-sign precession. (d) Dipolar anisotropy of coupling to the central spin (black dot). (e) Illustration of the spin texture for quantization axis aligned with the spiral wave vector, $\boldsymbol{Q} \parallel \boldsymbol{\eta}$. (f) Illustration of the dipolar interaction, spatially modulated at the pitch of the spiral for a case where the quantization axis is parallel to the gradient direction, $\delta\chi_{\boldsymbol{Q}\parallel\boldsymbol{\eta}}(\boldsymbol{r})$. (g) Measurement of spin-spiral dynamics for $\boldsymbol{Q}\parallel\boldsymbol{\eta}$. (h) Illustration of the spin texture for quantization axis perpendicular to the spiral wave vector, $\boldsymbol{Q} \perp \boldsymbol{\eta}$. (i) Corresponding spatial modulation of the dipolar interaction for the case where the quantization axis is perpendicular to the gradient direction, $\delta\chi_{\boldsymbol{Q}\perp\boldsymbol{\eta}}(\boldsymbol{r})$, sourcing an exchange field of opposite sign. (j) Opposite-sign, slower spiral precession measured for $\boldsymbol{Q} \perp \boldsymbol{\eta}$. (k) Measured precession frequency as a function of geometric anisotropy $\hat{\boldsymbol{Q}}\cdot\hat{\boldsymbol{\eta}}$ for $Q = 2\pi/(0.242\ \mu\text{m})$, showing tunable strength and sign of the exchange field. The solid line is proportional to the dipolar anisotropy $A_{\hat{\eta}}(\hat{\boldsymbol{Q}}) = (3(\hat{\boldsymbol{Q}}\cdot\hat{\boldsymbol{\eta}})^2 - 1)/2$ theoretically expected; see Supplemental Material [34], Sec. G1.

where the second term does not drive any dynamics, since it is aligned to the central spin orientation, and the first term determines the observed precession speed which is proportional to the effective *exchange field strength*

$$\omega \propto \chi_{\boldsymbol{Q}} = \int d\boldsymbol{r}\rho(\boldsymbol{r})\delta\chi_{\boldsymbol{Q}}(\boldsymbol{r}) \equiv \int d\boldsymbol{r}\rho(\boldsymbol{r})\frac{\mathcal{A}_{\hat{\boldsymbol{\eta}}}(\hat{\boldsymbol{r}})}{r^3}\frac{1-\cos(\boldsymbol{Q}\cdot\boldsymbol{r})}{2}, \tag{7}$$

where $\rho(\boldsymbol{r})$ is the coarse-grained spin density distribution and $\delta\chi_{\boldsymbol{Q}}(\boldsymbol{r})$ is the effective coupling sourced by a spin at distance $\boldsymbol{r}$. This exchange field produces a torque $\mathcal{T}$ leading to interaction-driven precession as depicted in Figs. 3(b) and 3(c). In this work, we experimentally determine the early-time precession rate ω by performing a linear fit of the measured spin precession angle as a function of interaction time.

Equation (7) can be interpreted as *modulating* the dipolar anisotropy with the factor $(1-\cos(\boldsymbol{Q}\cdot\boldsymbol{r}))/2$. This spatial modulation is plotted in Figs. 3(f) and 3(i) for the case of $\boldsymbol{Q}\parallel\boldsymbol{\eta}$ and $\boldsymbol{Q}\perp\boldsymbol{\eta}$, where $\hat{\boldsymbol{\eta}}$ is the quantization axis setting the dipolar anisotropy and $\hat{\boldsymbol{Q}}$ determines the modulation direction. For the case of $\boldsymbol{Q}\parallel\boldsymbol{\eta}$, the negatively interacting pairs (blue region) are suppressed by the modulation factor, leaving the positively interacting pairs (red region) dominating $\chi_{\boldsymbol{Q}}$ [Fig. 3(f)]. Conversely, in the $\boldsymbol{Q}\perp\boldsymbol{\eta}$ case, the positively interaction pairs are suppressed, leading to a $\chi_{\boldsymbol{Q}}$ with opposite sign [Fig. 3(i)]. We emphasize that this mechanism enables a nonzero spin precession rate in a 3D dipolar ensemble, despite the dipolar anisotropy that averages the Ising contribution to zero.

We experimentally test this expectation by tuning the direction of $\boldsymbol{Q}$ via the current ratio on the two microwires in Fig. 1(c) and comparing the measured spin precession. As shown in Figs. 3(g) and 3(j), we observe opposite precession directions for the $\boldsymbol{Q}\parallel\boldsymbol{\eta}$ and the $\boldsymbol{Q}\perp\boldsymbol{\eta}$ case, consistent with expectations. We further continuously tune $\hat{\boldsymbol{Q}}$ between these two directions. The data are plotted versus $\hat{\boldsymbol{Q}}$ direction in Fig. 3(k) and show excellent agreement with Eq. (7) (solid line).

Next, we contrast the spin precession measured under the native dipolar interaction and the Floquet engineered SU(2) Hamiltonian [Figs. 2(h) and 2(i)]. Here, we find two main differences: First, the native dipolar interaction yields a faster early-time precession [note the horizontal scale difference in Figs. 2(h) and 2(i)]. Second, the SU(2) symmetric Hamiltonian leads eventually to a larger precession amplitude. The first point results from Floquet engineering rescaling the exchange term of the Hamiltonian [35]—which drives spin-spiral precession—by a factor of $1/3$. To explain the second point, we note that the enhanced SU(2) symmetry leads to additional conservations of $\sum_i S_i^x$ and $\sum_i S_i^y$, which protects the transverse spiral order from local relaxation. This mechanism gives the spin ensemble more time to accumulate its precession dynamics before decaying, therefore leading to a larger precession amplitude. A continuous sweep of different XXZ Hamiltonians from easy axis to easy plane is presented in Supplemental Material [34] (Fig. S3), lending direct evidence to the SU(2) symmetry-based mechanism as generating the largest precession amplitude. Consequently, for the remainder of this work, we focus on the case of SU(2) symmetric interactions.

V. MICROSCOPIC POLARIZATION DRIVING SPIRAL DYNAMICS

The spin-exchange mechanism described above suggests that many-body dynamics can be tuned through the spiral pitch $\boldsymbol{Q}$ [see Eq. (7)]. After exploring the role of wave vector direction, we now vary its magnitude. Specifically, we extract the early-time spiral precession frequency ω as a function of wave vector magnitude [Fig. 4(c)], for the bulk diamond device [Fig. 1(c)]. The measured precession rate rises rapidly, then saturates, and eventually decays at larger wave vectors. To identify the characteristic length scale at which saturation occurs, we exploit a different imaging axis $\hat{\boldsymbol{Q}}'$ [see green arrows in Figs. 4(a) and 4(b)]. From the polarization profile [Fig. 4(d)] measured through FMI, we observe NVs confined axially by the sample thickness (185 nm), consistent with a fit to raw data in the Fourier space [inset in Fig. 4(d)]. Connecting those two experimental results, we finally note that the saturation in interaction-driven spiral dynamics occurs around $Q = 2\pi/(0.185\ \mu\text{m})$) [dashed line in Fig. 4(c)], indicating sensitivity to the extent of polarized region in the sample (here, the thickness of the NV layer).

To further corroborate these results, we study spiral dynamics on the nanobeam device [Fig. 1(d)]. Using the first NV group [indicated by a blue arrow in Fig. 4(b)], we measure spiral precession amplitude versus Q [Fig. 4(e)], which in this case probes the exchange field strength [Eq. (7) and Supplemental Material [34], Sec. G2]. The precession amplitude shows initial increase, saturation, and decay, with saturation occurring again at the scale of the polarized region [here, 300 nm width of the beam, dashed line in Fig. 4(e)].

Notably, we find that the saturation wave vector depends on the optical pumping duration [inset in Fig. 4(e)] as we probe the dynamics for two shorter optical pumping times τ [pumping time normalized by the calibrated saturation time τ_{sat}; see Supplemental Material [34] and Ref. [39]]. This is in contrast to the results from a bulk sample device [compare dark and light blue points in Fig. 4(c)].

We again elucidate these observations by FMI. Taking an image perpendicular to the nanobeam axis [green arrow in Figs. 4(b) and 4(f)], we reveal a dip in the polarization profile arising from nanophotonic interference of the pump light, confirmed by electric field simulations (Supplemental Material [34], Sec. A). Simulated NV polarization profiles [Fig. 4(g)] show that short pumping creates two lobes, which merge into a uniform profile with longer pumping, changing the extent of microscopic polarization. Those experimental results further point to the sensitivity of the many-body spiral dynamics to the system size.

To understand this feature of dipolar many-body dynamics, we analyze $\chi_{\boldsymbol{Q}}$ [Eq. (7)] for a spherical region of polarized spins with radius R_* [Fig. 4(h)]. For $Q = 0$ [first panel in Fig. 4(h)], all spins are aligned with the central

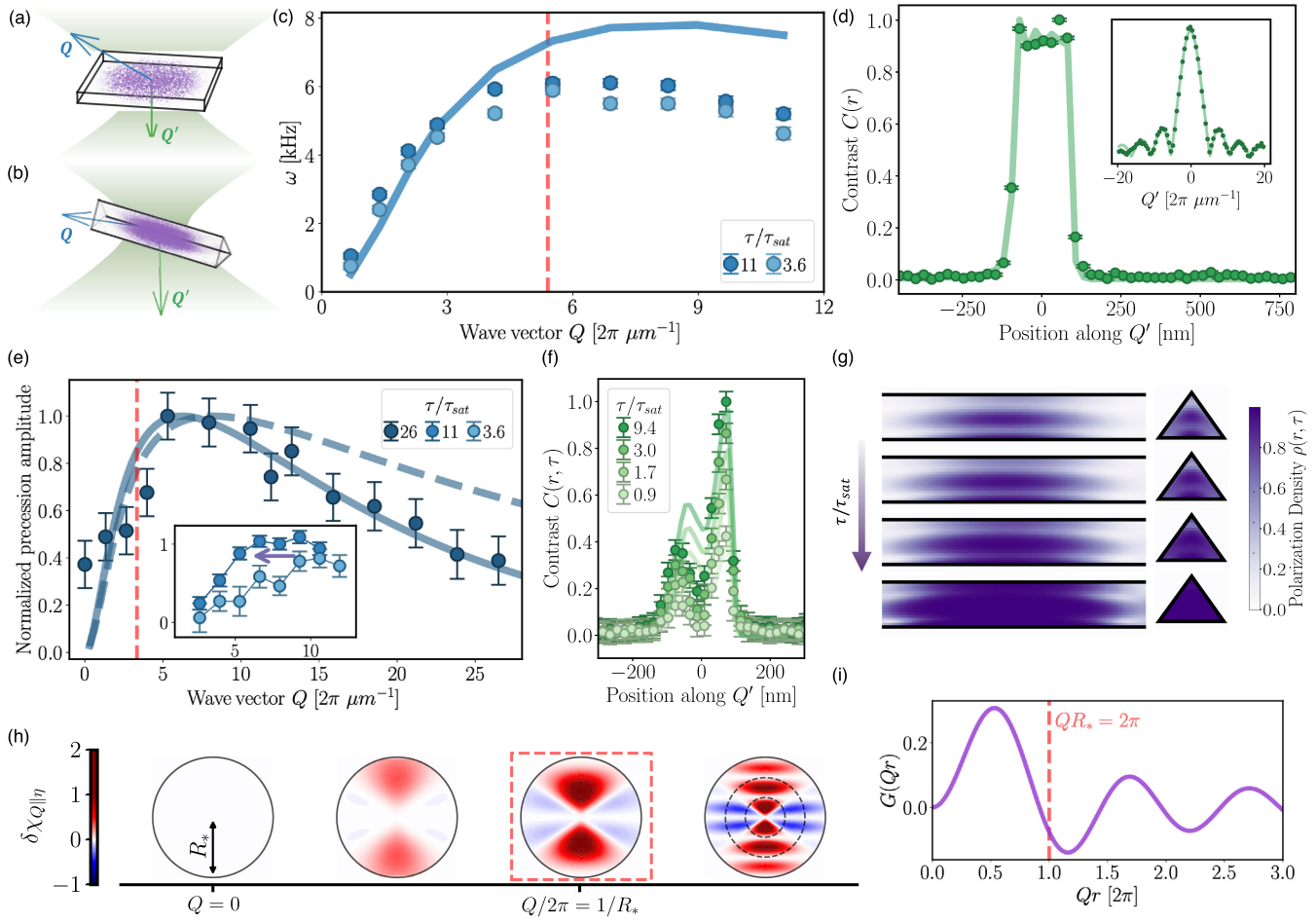


FIG. 4. Magnetic imaging of microscopic polarization driving spiral dynamics. (a) Spin polarization geometry in bulk diamond: disk-shaped region set by NV layer thickness (axial) and optical pumping (transverse). Gradient directions for spiral dynamics in (c) (blue) and imaging in (d) (green) are indicated. (b) Analogous geometry in the nanobeam device. Gradient directions for spiral dynamics in (e) (blue) and imaging in (f) (green) are indicated. (c) Measured spiral precession frequency ω versus wave vector Q in bulk diamond. Vertical line: $Q = 2\pi/(0.185\ \mu\text{m})$. Solid lines are theory predictions. (d) FMI taken across the bulk sample, used to extract NV layer thickness (185 nm). Inset: raw imaging data versus Q', with fit assuming a rectangular polarization profile. (e) Maximum normalized precession amplitude measured versus Q for NV group 1 in the nanobeam device. Vertical dashed line: $Q = 2\pi/(0.3\ \mu\text{m})$. Theory: dashed line—ideal spiral; solid line—with measured spiral winding loss (see Supplemental Material [34]). Inset: amplitude measured versus Q for shorter optical pumping times, showing saturation shift toward smaller wave vectors consistent with larger polarization extent. (f) FMI along the nanobeam short axis, revealing nanoscale polarization variations from nanophotonic interference. Experimental data are shown as markers; the solid line represents nanophotonics model predictions. (g) Theory cross sections of NV polarization in the nanobeam for increasing pump times. Spatial structure arises from optical interference of the green pump light. (h) Effective exchange coupling sourced by an isotropic polarization region with radius R_*, for spirals of varying pitch ($\boldsymbol{Q} = Q\hat{\boldsymbol{\eta}}$ for $QR_*/2\pi = 0, 0.4, 1, 3$). Dashed circles indicate shells of equal distance from a central spin, used to obtain $G(Qr)$ in (i). (i) The radial weighting function $G(Qr)$ as calculated via the angular averaging in Eq. (8).

spin; consequently, there is no exchange field and no resulting many-body dynamics.

For $Q/2\pi \ll 1/R_*$ (second panel), the mean field is strongly suppressed by the modulation factor $(1-\cos(\boldsymbol{Q}\cdot\boldsymbol{r}))/2$ in Eq. (7), leading to negligible $\chi_{\boldsymbol{Q}}$. With increasing Q toward $2\pi/R_*$ (third panel), contributions from distant spins are less and less limited by the modulation factor, leading to increasing $\chi_{\boldsymbol{Q}}$. Upon further increase of Q (fourth panel), dipolar anisotropy cancels the contribution from outer shells, leaving $\chi_{\boldsymbol{Q}}$ dominated by an inner core with radius $r = 2\pi/Q$, within which the modulation factor is effective at creating an imbalance of positively and negatively contributing spins. The number of contributing spins in this rescaled region ($\propto r^3$ for a 3D ensemble) balances the mean-field strength from each spin ($\propto 1/r^3$ for dipolar interaction), leading to a saturated $\chi_{\boldsymbol{Q}}$ beyond $Q = 2\pi/R_*$.

The above intuition is supported by integrating the exchange mean-field Eq. (7) in radial coordinates (see Supplemental Material [34], Sec. G3, which includes

Refs. [40–42] for analysis):

$$\chi_{\boldsymbol{Q}} = \rho \int_0^{R_*} dr 4\pi r^2 \frac{1}{r^3} G(Qr) A_{\hat{\boldsymbol{\eta}}}(\hat{\boldsymbol{Q}}), \tag{8}$$

where ρ is the polarization density, $4\pi r^2 dr$ is the volume measure, $1/r^3$ arises from dipolar interaction, and $G(Qr)A_{\hat{\boldsymbol{\eta}}}(\hat{\boldsymbol{Q}})$ arises from the integral over the 4π solid angle

$$G(Qr)A_{\hat{\boldsymbol{\eta}}}(\hat{\boldsymbol{Q}}) = \int \frac{d\hat{\boldsymbol{r}}}{4\pi} A_{\hat{\boldsymbol{\eta}}}(\hat{\boldsymbol{r}})(1 - \cos(\boldsymbol{Q}\cdot\boldsymbol{r})). \tag{9}$$

The function $G(Qr)$ is plotted in Fig. 4(i) and physically represents the effective weighting of each shell of polarization [dashed circles in Fig. 4(h)] to the net exchange field, as encoded by the shell radius in units of spiral wavelength.

A crucial observation in Eq. (8) is that the effective radial measure dr/r is *scale invariant* under $r \to r/Q$. This property arises from the matching spatial dimension ($D = 3$ sets the volume measure) and the dipolar decay exponent ($1/r^\alpha$ with $\alpha = 3$). As a consequence, it is convenient to define a dimensionless variable $x \equiv Qr$, which transforms Eq. (8) to

$$\chi_{\boldsymbol{Q}} = 4\pi\rho A_{\hat{\eta}}(\hat{Q}) \int_{Qa}^{QR_*} \frac{dx}{x} G(x), \tag{10}$$

where the effect of sweeping Q is exclusively encoded in the limits of the integral. As shown in Fig. 4(i), the function $G(x)$ oscillates as $x \to \infty$, which cures the logarithmic divergence associated with $\int[(dx)/x]$. Furthermore, the first lobe of $G(x)$ appears between 0 and 2π, explaining why $Q = 2\pi/R_*$ is the wave vector at which $\chi_{\boldsymbol{Q}}$ saturates.

Additional insight can be gained by recalling that the dipolar interaction kernel derives from the Coulomb potential [43] as

$$\frac{A_{\hat{\boldsymbol{\eta}}}(\hat{\boldsymbol{r}})}{r^3} = (\hat{\boldsymbol{\eta}}\cdot\nabla)^2 \frac{1}{r} + \frac{4\pi}{3}\delta(\boldsymbol{r}), \tag{11}$$

which under a Fourier transform (approximately imparted by the spiral texture) is mapped as

$$\to (\hat{\boldsymbol{\eta}}\cdot i\boldsymbol{k})^2 \frac{4\pi}{k^2} + \frac{4\pi}{3} = -\frac{4\pi}{3} A_{\hat{\boldsymbol{\eta}}}(\hat{\boldsymbol{k}}), \tag{12}$$

resulting in a *gapped scaling* [i.e., $A_{\hat{\boldsymbol{\eta}}}(\hat{\boldsymbol{r}})/r^3 \to \mathcal{O}(k^0)A_{\hat{\boldsymbol{\eta}}}(\hat{\boldsymbol{k}})$ as $k \to 0$] when neglecting the short- and long-distance regulation of the spiral texture considered above. This sensitivity to the microscopic extent in saturating this gap is, thus, a fundamental property of the dipolar interaction in three dimensions [36], as borne out in our experiments performed on two distinct samples [Figs. 4(c) and 4(e)].

VI. COHERENT, COLLECTIVE DYNAMICS IN A DISORDERED DIPOLAR SPIN SYSTEM

We next explore the long-time dynamics of the spin spirals on the bulk sample device [Fig. 1(c)]. Specifically, we prepare spin spirals with different cone angles θ [Fig. 5(a)] and monitor their evolution at $Q = 2\pi/(0.242\ \mu\text{m})$, where the spin-exchange field is strongest [Fig. 4(c)]. We perform tomography by measuring all components of the collective spin, and we depict the resulting time evolution on the Bloch sphere [Fig. 5(a), where points become more transparent as the evolution proceeds]. Additionally, we experimentally observe a linear growth of the precession angle ϕ [Fig. 5(b)], defined as

$$\langle S^+_{\boldsymbol{Q}}(t)\rangle = e^{i\phi(t)}|\langle S^+_{\boldsymbol{Q}}(t)\rangle| \tag{13}$$

with a rate [extracted through linear fit to data in Fig. 5(b)] that exhibits a cosine dependence upon the cone angle θ, consistent with the S^z-proportional precession frequency [Fig. 5(c)], where $S^z \equiv \sum_j S^z_j$ is the collective spin. These observations closely resemble the nonlinear dynamics generated by the one-axis twisting (OAT) Hamiltonian [6] for N spins, $H_{\text{OAT}} = \chi(S^z)^2/N$, with an effective twisting rate $\chi = \chi_{\boldsymbol{Q}} = 8.51(2)$ kHz. We further study this metrologically useful dynamics by measuring the maximum spiral twisting amplitude for different interaction types [Fig. 5(d)]. SU(2) engineered interactions (purple points) produce a large twisting—considerably exceeding values resulting from both the native interaction Hamiltonian (orange points) as well as those measured previously in similar systems [26,27]. High quality of this dynamics is also evident in a pronounced asymmetry toward larger cone angles [Fig. 5(d)] that reflects the curvature of the collective Bloch sphere (Supplemental Material [34], Sec. G4).

To understand these observations, we note that, in the recent studies of two-dimensional disordered systems [26,27], twisting dynamics were found to be limited by strongly interacting spin pairs which induce a large energy scale that dominates the local dephasing [top, Fig. 5(e)]. To understand why such contribution is regulated in our case, we note that nearby spin pairs in a long-wavelength spiral are approximately collinear [bottom, Fig. 5(e)]. Under an SU(2)-symmetric Hamiltonian, such nearly collinear pairs do not contribute appreciably to the many-body relaxation dynamics, rendering the spiral dynamics insensitive to local dynamics in these strongly coupled pairs, or other microscopic details. More generally, the spin spirals employed here form slow, hydrodynamic modes of the many-body system under SU(2)-symmetric interactions [44,45]. These modes remain protected from relaxation up to the macroscopic spin-transport timescale, which is set by the tunable spiral wavelength $2\pi/Q$ and the transport universality class of the dipolar Heisenberg model [36]. To probe this experimentally, we measure the time evolution of the spiral amplitude $|\langle S^+_{\boldsymbol{Q}}(t)\rangle|$ for different spiral wave vectors $\boldsymbol{Q}$

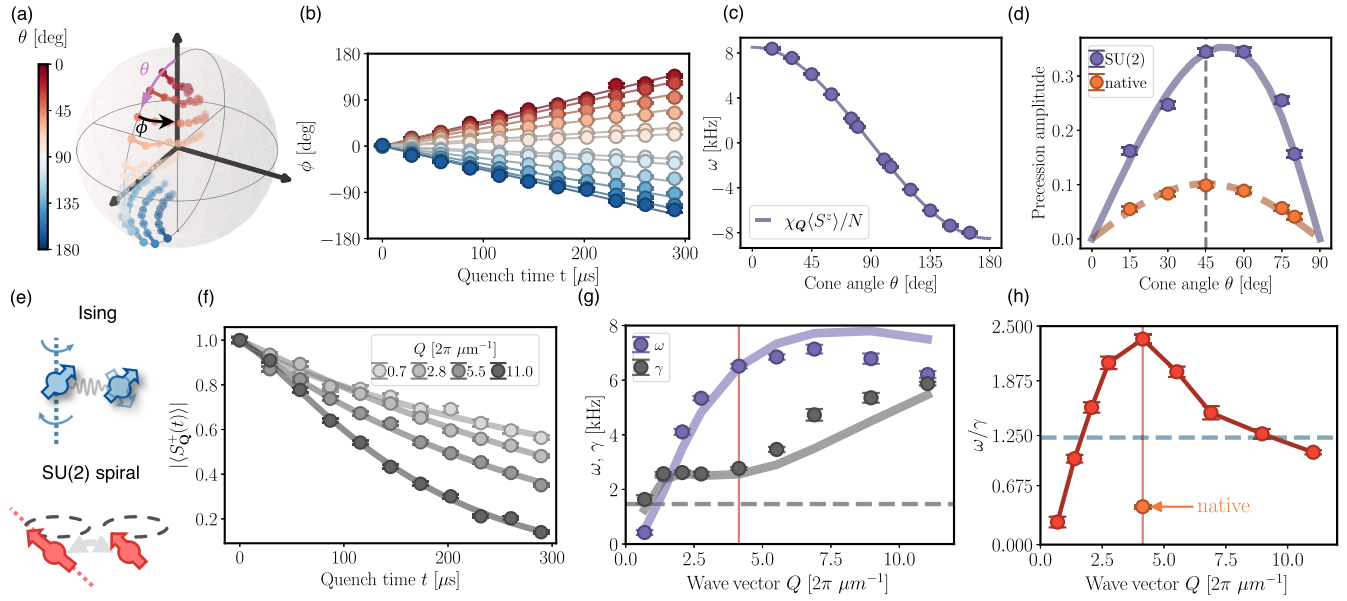


FIG. 5. Collective nonlinearity in a disordered, three-dimensional dipolar spin system. (a) Measured dynamics of spin spirals prepared at cone angle θ and precessing by angle ϕ. Most transparent point marks maximum quench time $t = 289.44$ μs. Plotted points are a result of tomography measurement of total spin after unwinding the spiral, following different quench times. Data used in (b)–(d) were collected with improved drive and gradient homogeneity at $Q = 2\pi/(0.242\ \mu\text{m})$, shown by the thin red line in (g),(h). (b) Measured spiral precession angle ϕ versus quench time for a range of initial cone angles θ. Solid lines are linear fits used to extract ω in (c). (c) Extracted precession rate of the spiral versus cone angle θ. The fitted cosine dependence (solid line) is characteristic of OAT dynamics. (d) Measurement of interaction-driven precession amplitude versus cone angle θ (markers) for different forms of interactions. Purple line: numerical simulations multiplied by measured decoherence [Fig. S1(b) [34]]. Dashed orange line: naive model $\propto \sin(\theta)\cos(\theta)$. (e) Illustration of a pair of strongly coupled spins. In the Ising case, local interactions and quantum fluctuations lead to fluctuating $\hat{z}$ field (vertical dashed line), causing random precession (curved arrows) and fast dephasing. For a long-wavelength spiral evolving under an SU(2) Hamiltonian, nearby spins contribute a field nearly aligned (red dashed line) with the target spin, preventing local dephasing. (f) Decay of the spiral amplitude for conical spiral with $\theta = 45°$ at varying wave vectors evolving under SU(2) Hamiltonian. Solid lines are fits to stretched exponential decay. (g) Precession frequency ω and decay rate γ measured as functions of the spiral wave vector Q for SU(2) interaction. The horizontal dashed line marks the extrinsic decay rate; solid lines denote theoretical predictions (Sec. VIII K). (h) Many-body dynamics quality factor ω/γ computed from (g). The horizontal dashed line indicates the theoretical maximum for a two-dimensional Ising model of dilute, positionally disordered spins with unity spin polarization, while an orange marker indicates the measured quality factor for native interactions. Experimental points are connected by lines as a guide to the eye.

[Fig. 5(f)]. Here, we observe a markedly slower decay of the spiral amplitude for longer spiral wavelengths, manifesting the protection of spiral modes.

We note here that the effects of interactions are twofold: First, the mean-field exchange leads to OAT-like dynamics [Fig. 5(a)]. Second, the dipolar interaction leads to dephasing and the decay of the polarization [Fig. 5(f)]. The interplay of these mechanisms governs the quality of the many-body dynamics. Experimentally, we compare the fitted spiral decay rate γ with the precession frequency ω in Fig. 5(g) and find a striking separation of scales. The maximum separation occurs when the spiral pitch is comparable to the inverse linear system size [Fig. 5(g)], beyond which ω saturates but γ keeps increasing, consistent with theoretical predictions [solid lines in Fig. 5(g)]. In Fig. 5(h), we explicitly plot the quality factor ω/γ—a direct measure of the collectivity of the nonlinear dynamics (see Supplemental Material [34], Sec. G4)—versus spiral pitch and compare it with the analytic limit set by local dynamics in a dilute, positionally disordered two-dimensional Ising model, predicting maximum $\omega/\gamma = \sqrt{3/2} \sim 1.22$ (dashed line; see Supplemental Material [34], Sec. G4, and Ref. [46] for derivation). While for the system with native interactions quality factor is below this limit, in the case of SU(2) interactions, our observations clearly exceed this limit for a broad range of wave vectors, demonstrating collective nonlinear dynamics in a positionally disordered dipolar system.

VII. DISCUSSION AND OUTLOOK

Twisting dynamics with *all-to-all* Ising interactions provides the simplest, textbook example of collective nonlinearity from Ising interactions among N spins, with a quality factor $\omega/\gamma = \mathcal{O}(\sqrt{N})$, capable of generating scalable amplification and spin squeezing [6]. By contrast, generic short-range Ising interactions yield a quality factor that does not scale with system size, $\omega/\gamma = \mathcal{O}(1)$ [47]

[dashed line in Fig. 5(h) for a dilute dipolar system; see Supplemental Material [34], Sec. G4]. The use of spin spirals allows us to surpass this limit [Fig. 5(h)] with a substantially larger quality factor via SU(2)-symmetry engineering of dipolar interactions. Theoretical analysis (see Ref. [36] and Supplemental Material [34], Sec. G4) predicts that, in isolated, disordered dipolar systems, such spiral-mediated twisting can, in principle, achieve an ideal $\mathcal{O}(\sqrt{N})$ quality factor due to the separation of timescales between spiral relaxation and exchange-driven twisting. Specifically, for dipolar interactions in three dimensions, one expects the twisting rate ω to be independent of the system size—provided the spiral wave vector is tuned to the inverse system size, $Q_* = \mathcal{O}(1/R_*) = \mathcal{O}(1/N^{1/3})$ [red line in Figs. 5(g) and 5(h)]—while the relaxation rate γ is parametrically slower in larger systems due to emergent spin hydrodynamics [36], resulting in collective, scalable twisting dynamics directly from dipolar interactions.

Our experiments demonstrate that nanoscale magnetic field gradients induce emergent collective dynamics in disordered dipolar ensembles. While magnetic gradients have been used previously to probe dipolar interactions in nuclear spin ensembles [48–50], it is the combination with Floquet-engineered SU(2)-symmetric interactions [35,36,38] that mitigates the effects of disorder, engineering coherent collective dynamics. In particular, we have shown that the far-from-equilibrium relaxation of long-wavelength spin spirals under SU(2)-symmetric dipolar interactions generates coherent OAT-like dynamics.

These results can be extended along several directions. Probing intrinsic spiral relaxation and its connection to emergent spin hydrodynamics can provide new insights into the dynamics of such a complex system [51–53]. While related phenomena have been explored in electronic and nuclear spin-1/2 systems [54,55], ultracold atoms [33,56–59], and spin-orbit-coupled semiconductors [60,61], our platform offers distinct features, including tunable SU(2) symmetry, long-range interactions, magnetic frustration, and intrinsic positional disorder, allowing for spatially resolved studies of such complex quantum many-body dynamics [62–64].

At the same time, the disorder-robust collective nonlinearity observed here can further be applied to realize interaction-enhanced metrology. With long coherence times [65] and high-fidelity readout [23], entanglement generation and spin squeezing [36] become feasible, while scalable signal amplification [26,66] promises substantial sensitivity gains in practical magnetic sensing tasks [67]. Exploiting long-wavelength spiral textures and Hamiltonian engineering, we introduced a mechanism to regulate positional disorder that extends beyond methods based on depolarizing strongly coupled spins [27], thus preserving the density of quantum sensors and associated magnetic sensitivity [22]. This is particularly relevant since the experimental platform introduced here is a prime candidate for a nanoscale magnetic resonance imaging [68] system, owing to its high spatial resolution (below 20 nm in this work) inherited directly from the high spin density and strong gradients. Those versatile imaging capabilities can be further extended making use of multiplexed detection [69] and compressed sensing [24,70] and applied to measure spatiotemporal correlations [24,71], naturally complementing the intrinsic magnetic sensing modalities of dense NV ensembles [22,23]. Together, these results establish a versatile platform for nanoscale sensing and magnetic imaging, with quantum advantage within reach under ambient conditions.

VIII. METHODS

A. Gradient chip

1. Nanobeam device

To generate strong magnetic field gradients and a microwave (MW) drive for the ensemble of dipolar spins in a diamond nanobeam, a custom, two-layer chip was fabricated following a series of steps.

(i) *Substrate preparation*—Silicon carbide substrates (23 mm × 23 mm × 0.35 mm) were cleaned with acetone, isopropanol (IPA), piranha solution (H_2SO_4: H_2O_2, 4∶1), buffered hydrofluoric acid (5∶1), and oxygen plasma (100 W, 40 sccm, 1 min) to remove organic residues, surface oxides, and enhance resist adhesion.

(ii) *Gradient coil fabrication*—Two layers of polymethyl methacrylate (PMMA) resist (PMMA 495K followed by PMMA 950K) were spin-coated onto the substrate. A conductive espacer layer was deposited to mitigate charging during electron beam lithography. Gradient coils were defined by electron beam lithography and developed in MIBK:IPA (1∶3). A descum step was performed using oxygen plasma. A metal stack of chromium (Cr, 10 nm) and gold (Au, 500 nm) was deposited by electron beam evaporation. Liftoff was performed in Remover PG with mild ultrasonication.

(iii) *Dielectric spacer deposition*—An alumina (Al_2O_3) layer (30 nm) was deposited by atomic layer deposition. A silicon dioxide (SiO_2) layer (500 nm) was deposited by plasma-enhanced chemical vapor deposition (CVD).

(iv) *Ω-loop fabrication*—Two layers of resist (LOR20B followed by S1813) were spin-coated onto the sample. The Ω loop was patterned using a maskless lithography aligner, aligned to features near the device center. After development, a Cr (10 nm)/Au (700 nm) metal stack was deposited by electron beam evaporation. Liftoff was performed in Remover PG.

(v) *Contact pad opening*—A photoresist (S1818) was spin-coated to define the bonding pad openings. Exposed dielectric layers were removed by buffered

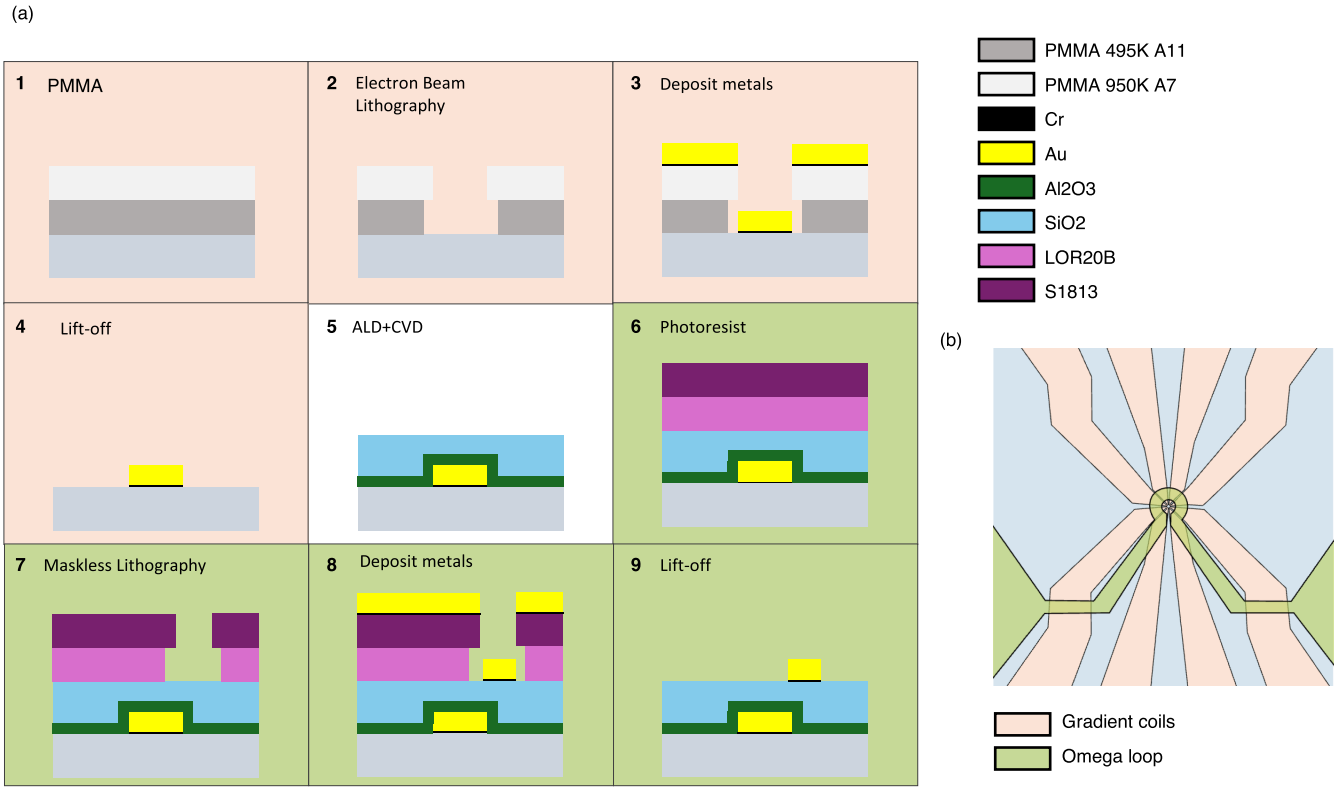


FIG. 6. Gradient chip fabrication. (a) Two-layer gradient chip fabrication process divided into nine steps. Different material layers are indicated by different colors. (b) Design of the fabricated gradient chip. The two layers—containing the gradient coils and the Ω loop used for MW driving—are highlighted.

oxide etch (BOE). A final cleaning step was performed in Remover PG.

The fabrication steps, as well as the overall chip design, are shown in Fig. 6. The fabricated chip under white light and confocal microscope is shown in Figs. 7(a) and 7(b). The design of the chip allows for a switchable current to be applied through any of the four small constrictions, enabling a time-dependent magnetic field gradient [Figs. 7(d) and 7(e)]. On the second layer of the chip, an Ω loop is patterned, which is used to coherently drive spins, allowing for disorder decoupling and Floquet engineering of a desired form of an interaction Hamiltonian.

2. Bulk diamond device

To apply a microwave drive and a switchable gradient to bulk diamond, a single-layer chip was fabricated. The design [Fig. 7(f)] consists of two pairs of differential lines narrowing down in the central 50 μm region to four gold wires, with widths of 10, 5, 5, and 10 μm and with equal gaps of 6 μm between the wires. In the experiment, only a single pair of coils is used at a time: The inner pairs are suitable for producing the strongest magnetic field gradient, while the outer pairs yield a more linear gradient. The coil was fabricated in the following steps.

(i) *Substrate preparation*—A polycrystalline CVD diamond substrate (25 mm × 25 mm × 0.13 mm) was sonicated in acetone first, followed by IPA sonication.

(ii) *Coil fabrication*—Two layers of photoresist (LOR 20B followed by S1813) were spin-coated onto the substrate. The coil pattern was defined by photolithography and developed in MF-319. A metal stack of titanium (Ti, 20 nm), gold (Au, 860 nm), and titanium (Ti, 20 nm) was deposited by electron beam evaporation. Liftoff was performed in 80 °C Remover PG.

(iii) *Dielectric top-layer deposition*—An alumina (Al_2O_3) layer (40 nm) was deposited by atomic layer deposition for extra protection against electrical breakdown.

(iv) *Contact pad opening*—A layer of photoresist (S1818) was spin-coated onto the substrate. An etch mask for the bond pads was defined by photolithography and developed in MF-319. The exposed dielectric layer and top titanium layer were removed by buffered oxide etch (1:7 BOE). A final cleaning step was performed in Remover PG, followed by a rinse in acetone and IPA.

B. Interfacing PCB

Combing strong magnetic control and microwave drive requires an interfacing printed circuit board (PCB).

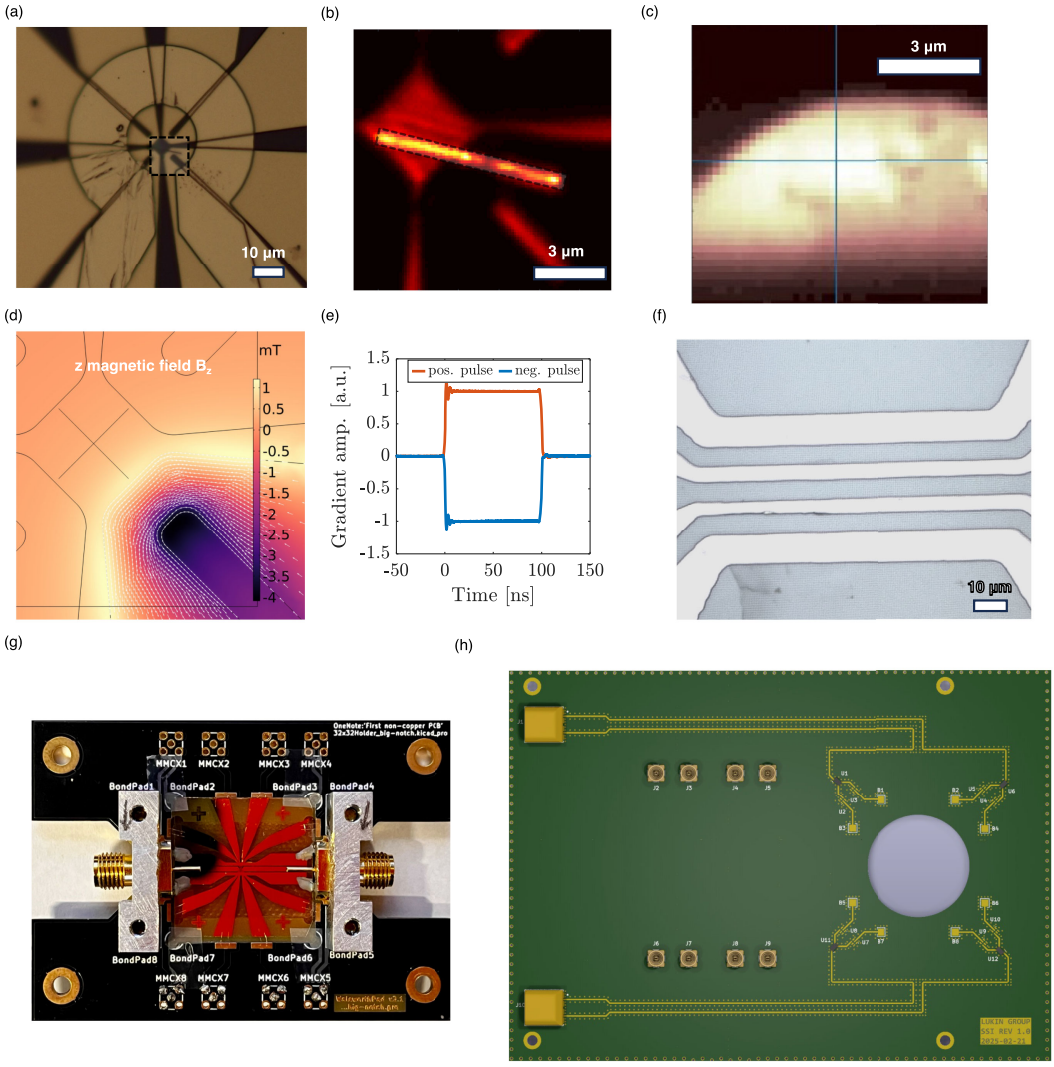


FIG. 7. Dynamic magnetic field gradients on the chip. (a) White-light image of the custom chip providing switchable magnetic gradients and MW control in a diamond nanobeam device. The thin, long beam is a diamond sample hosting the dipolar ensemble used in parts of this study. (b) Confocal image of the nanobeam on top of a gradient coil, highlighted with white light. (c) Confocal scan of the bulk device showing the dense NV spot between central microcoil wires. (d) Calculated gradient field at 1/10 maximum strength in the nanobeam device. (e) Dynamic control of the gradient field. Measured current traces for 100-ns positive and negative pulses. (f) Microscope image of the four-wire single-layer chip for bulk device; inner pairs yield stronger gradient, outer pairs more linear one. (g) Photograph of the two-layer gradient chip on a PCB in the nanobeam device. (h) PCB interfacing MW signals and gradient pulses for the single-layer chip, with central hole for laser access.

1. Nanobeam device

The two-layer chip is mounted on a simple PCB [see Fig. 7(g)] that interfaces the gradient and MW lines with the microcoil structure. For MW connections, SMA connector pins are electrically connected to the coplanar waveguide section of the chip using silver paste. Gradient coils are connected via wire bonds from the exposed contact pads on the chip to corresponding pads on the PCB, which are, in turn, connected to pins interfacing with the gradient pulser.

2. Bulk diamond device

For the single-layer chip, MW control signals are combined with the gradient pulses using a custom-built PCB [see Fig. 7(h)]. The PCB has a symmetric design: The 180°-shifted MW signals (Fairview Microwave FMCP1155 SMA 180 degree hybrid coupler) are fed into two ports on one side of the PCB, while the pair on the other end is terminated. The microwave signal passes through two baluns (TTM Balun Xinger X4BD40L1-50100G) and is then combined using four rf diplexers (Mini-Circuits LDPW-162-242+) with a lower-frequency gradient signal.

C. Diamond sample

The spin ensemble used in this work consists of spin-1 nitrogen-vacancy (NV) centers in diamond, where a ground-state transition $m_S = -1 \rightarrow m_S = 0$ is driven,

resulting in an effective spin-1/2 ensemble. Our work uses two different high-NV-density diamond samples.

1. Bulk sample

For most of this work, a bulk, CVD-grown, highly doped diamond sample is used [Fig. 7(c)]. The diamond sample was created in a following process. Diamond homoepitaxial growth and nitrogen doping were performed via plasma-enhanced chemical vapor deposition using a SEKI SDS6300 reactor on a (100)-oriented electronic grade diamond substrate (Element Six Ltd.). Prior to growth, the substrate was fine-polished by Syntek Ltd. to a surface roughness of approximately 200–300 pm, followed by a 4–5 μm etch to relieve polishing-induced strain. The growth conditions consisted of a 750 W plasma containing 0.5% $^{12}CH_4$ in 400 sccm H_2 flow held at 25 torr and approximately 730 °C according to a pyrometer. A 125-nm-thick isotopically purified (99.998% ^{12}C) buffer layer was grown, followed by a 185-nm-thick ^{15}N-doped layer (1 sccm $^{15}N_2$ gas) and a 100-nm-thick ^{12}C capping layer. After growth, the sample was characterized with secondary ion mass spectrometry to estimate the isotopic purity and epilayer thickness. The diamond was further electron irradiated and annealed to generate enhanced NV center concentrations. Irradiation was performed with the 200 keV electrons of a transmission electron microscope (TEM, ThermoFisher Talos F200X G2 TEM). The irradiation time was varied to create spots that range in dose from 10^{17} to 10^{21} e^-/cm^2, and the reported experiments are performed at one spot with irradiation dose 2.4×10^{19} e^-/cm^2. The sample then underwent subsequent annealing at 850 °C for 6 h in an Ar/H_2 atmosphere, during which the vacancies diffuse and form NV centers. After irradiation and annealing, the sample was cleaned in a boiling triacid solution (1:1:1 H_2SO_4: HNO_3: $HClO_4$) and annealed in air at 450 °C to oxygen terminate the surface and help stabilize the negative NV^- charge state for further measurements.

The density of NV centers in the confocal spot is estimated based on the $XY16$ decay timescale of 21.5 μs, corresponding to a single-group NV^- density of 246 ppb. The conversion between $XY16$ decay timescale and NV^- density is obtained empirically based on numerical simulations, assuming that the decay is dominated by dipolar interaction between NV centers.

2. Nanobeam sample

A piece of *black diamond* (approximately 3.8 ppm per NV group) characterized in earlier works [31] is used for the later part of this work [Fig. 7(b)]. The high density of NVs leads to strong magnetic dipole coupling ($J_{typ} \approx 35$ kHz) between spins, while strain and the presence of other defects result in strong on-site disorder ($W_{typ} \approx 4$ MHz), necessitating the use of decoupling sequences. The diamond sample is shaped into a triangular nanobeam (0.3×8 μm) and placed on top of the chip [see Figs. 7(a) and 7(b)]. Shaping the diamond into a nanostructure improves fluorescence collection, enhances the homogeneity of the Rabi drive, and enables the application of strong gradients with a well-defined direction $\mathbf{\nabla}$.

D. Initialization and readout

The NV spin state is initialized and read out using a custom-built confocal microscope operating under ambient conditions. Green laser light (532 nm) is focused onto the sample through a high-NA objective. The device is mounted on a piezo stage, which is used to control the position of the confocal spot and allows for $\hat{z}$ focusing. Red NV fluorescence is collected through the same objective and reflected by a dichroic mirror (which filters out the excitation light) toward a single-mode fiber acting as a pinhole to reject out-of-focus fluorescence. The collected fluorescence is then focused onto a pair of single-photon counting modules (bulk sample) or a multipixel photon counter module (nanobeam diamond) for measurements.

E. MW control

1. Bulk diamond device

For the bulk diamond device, MW pulses ($f = 2.3743$ GHz) are directly synthesized using an arbitrary waveform generator (AWG) Tektronix AWG7122C and amplified using Mini-Circuits ZHL-16W-43-S+.

2. Nanobeam device

For a nanobeam device, MW pulses ($f = 2.5036$ GHz) are generated via IQ mixing (Marki Microwave MMIQ-0205H) of signals from a microwave generator (Rohde&Schwarz SMC100A) and analog control pulses synthesized by the AWG (Tektronix AWG 7052). After IQ mixing, the MW signal is lowpass filtered (<3.2 GHz) to eliminate spurious harmonics and then amplified (Mini-Circuits ZHL-25W-63+). IQ leakage is minimized at the qubit frequency to prevent spurious driving between pulses.

F. Gradient control

The switchable gradient field is controlled by a custom field-programmable gate array (FPGA)-based current pulser, enabling short (>15 ns) current pulses with switchable polarity and an amplitude up to approximately 1.1 A [Fig. 7(e)]. The pulser consists of three main components (Fig. 8). First, the main board (controller board) generates low-noise, stable voltage references for each coil using ultralow-noise, ultrahigh-power supply rejection ratio linear regulators (Analog Devices LT3045), which are subsequently amplified by power operational amplifiers (Texas Instruments OPA564). First, the main board (controller board) provides a voltage driver for each coil based on reference voltages supplied to the pulser. These voltage drivers are implemented using either voltage regulators

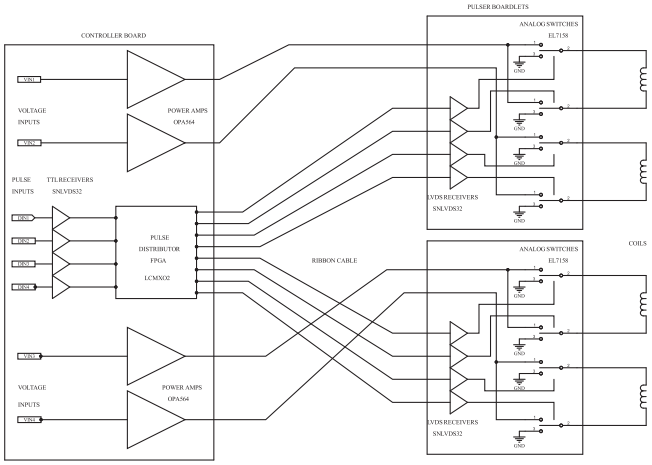


FIG. 8. Gradient pulser design. Schematics of the pulser used to create switchable magnetic field gradients.

(Analog Devices LT3045) or power operational amplifiers (Texas Instruments OPA564), depending on whether dynamic tracking of the reference voltages is required. On the same main board, the supplied transistor-transistor logic signals are processed using a programmable FPGA (Lattice Semiconductor Corporation LCMXO2), enabling flexible control over the polarity and switching of the pulses. Finally, two small daughter boards are connected to the main board, each containing a pair of noninverting quad CMOS drivers (Renesas EL7457), which serve as high-current, high-speed analog switches. The current pulses are triggered using marker channels from a high-sampling-rate AWG, allowing synchronization of gradient and MW pulses.

G. Addressing selected NV group

To address the $m_S = -1 \rightarrow m_S = 0$ transition in a particular crystallographic group of NVs, an external static magnetic field is applied to split the Zeeman levels of the NV ground state. The magnetic field is generated by a set of three perpendicular electromagnetic coils, and repeated ESR experiments are used to finely align the field direction with the quantization axis of each NV group. This alignment information is also used to transform the NV group orientations into the lab frame, which allows for the reconstruction of the relevant experimental geometry—namely, the orientation of $\boldsymbol{\eta}$ for each NV group. To improve readout contrast, the laser light polarization is adjusted individually for each NV group via a half wave plate.

H. Determination of gradient directions

1. Bulk diamond device

We determine the geometry of the pulsed magnetic field in the bulk sample device by measuring a series of ESR spectra with electric current applied to individual coils, as a function of position across the middle two wires near the working spot on the sample [see Fig. 1(e)]. By fitting the ESR spectra for all NV groups, we reconstruct the vector magnetic field at each spatial position and for each current configuration. The resulting position-dependent vector magnetic field is further fitted to a local quadratic model, to extract the field gradient within the NV plane. The out-of-plane components of the gradient are then inferred based on constraints from Maxwell's equations. This calibration procedure allows us to determine the appropriate current ratios in the individual wires required to achieve a desired magnetic field gradient direction and strength.

2. Nanobeam device

To determine the geometry of the magnetic field on a nanobeam device, we use finite-element method simulations of the magnetic field produced by the microcoil [Fig. 7(d)]. Additionally, we collect a series of confocal scans under extra white-light illumination, which highlights the edges of the microcoil [Fig. 7(b)], to extract the lateral and axial (z) position of the diamond nanobeam relative to the microcoil structure. We then use the simulated magnetic field and the best estimates of the beam position as input to an optimization procedure that compares the experimentally measured ESR detunings along the nanobeam with the predictions from simulations [see Fig. 1(f)]. In this optimization, we allow only for a translation of the nanobeam relative to the coil center and an overall scaling of the

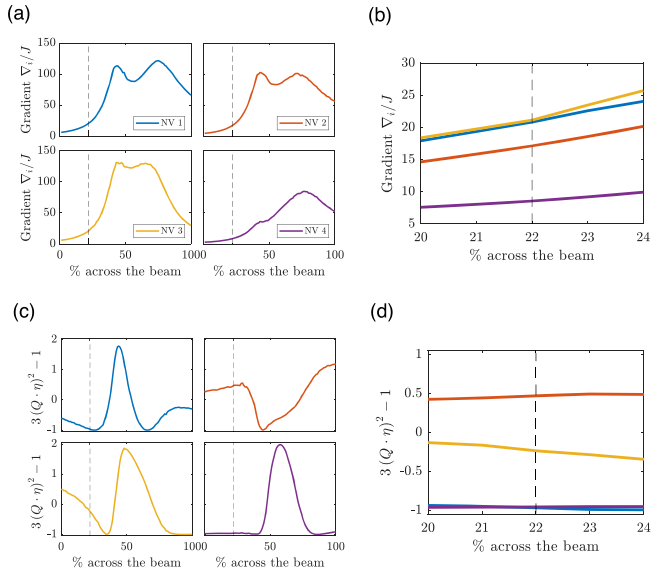


FIG. 9. Magnetic gradient geometry for a nanobeam device. (a) Gradient strength, in units of typical dipolar spin-spin coupling, across the nanobeam for all four NV groups. (b) Gradient strength in a narrow range near the working point. (c) Geometric factor determining the sign and strength of the dipolar mean field across the nanobeam for all four NV groups. (d) The same geometric factor near the working point. Dashed vertical lines correspond to a working point on the nanobeam—22% along its length.

magnetic field strength. This procedure results in a shift of less than 0.6 μm in the nanobeam position compared to the values extracted directly from the confocal scans. In this way, we obtain the magnetic field model used to determine the direction and strength of the effective gradient $\mathbf{\nabla}_\alpha$ used throughout this work (see Fig. 9).

I. Preparation of spin spirals

In this work, we prepare spin spirals by evolving NVs in an inhomogeneous magnetic field created by the gradient coils. In the nanobeam device, the strength of the gradient (∇_i) varies across the beam and NV groups and is plotted in Figs. 9(a) and 9(b) in units of dipole interaction strength. The interplay between interaction and gradient strength is important for the preparation of high-quality spin spirals; see Figs. S3(d) and S3(f) [34].

Spiral winding is implemented in two blocks separated by a π pulse on the spins, which allows for decoupling of static on-site magnetic disorder that would otherwise dominate over the local gradient field. To avoid transient

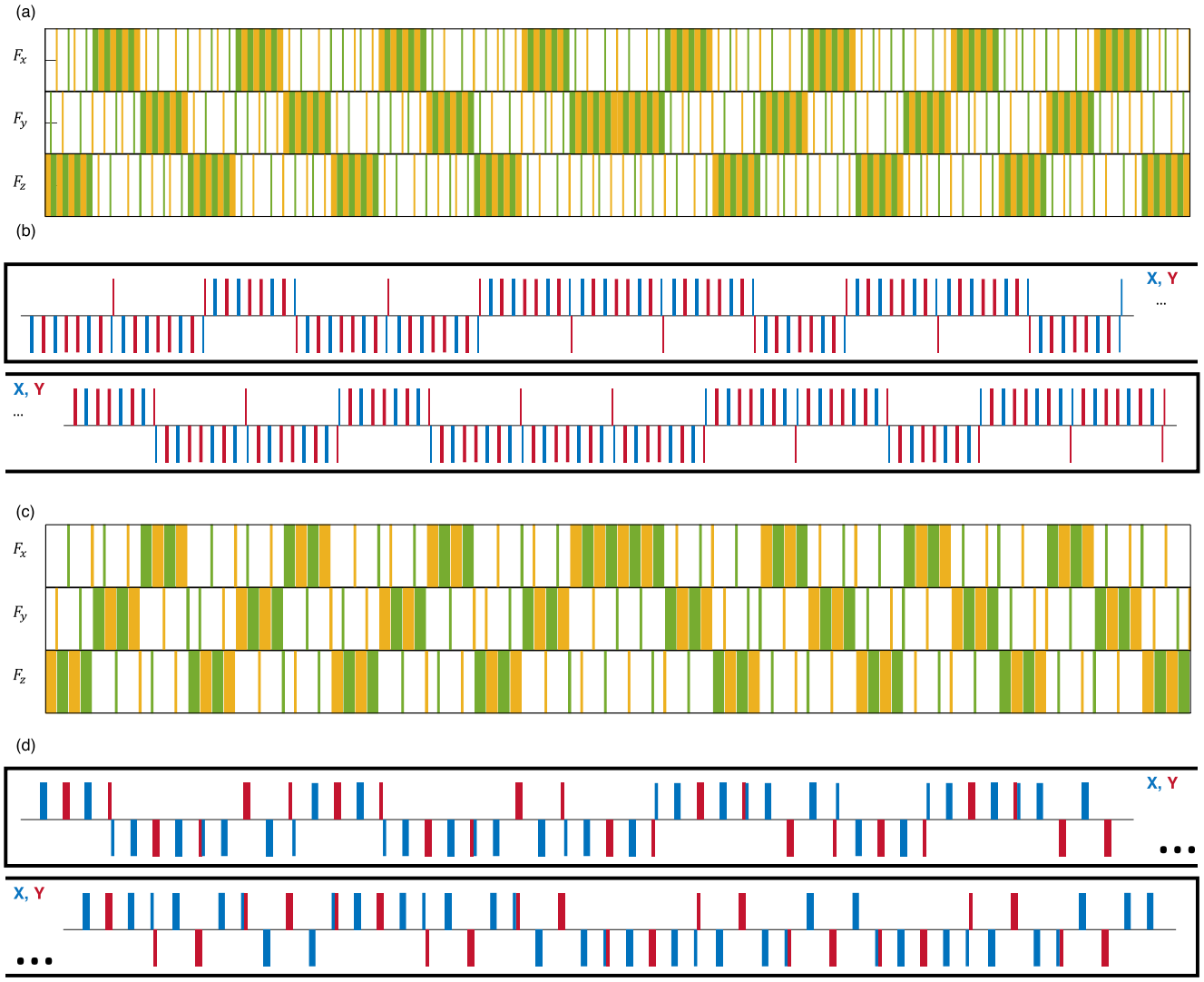


FIG. 10. Hamiltonian engineering pulse sequences. (a) Frame representation [38] of the pulse sequence "cXY8-DROID-vXY4-Mirror" used for the bulk sample device, showing the concatenated structures discussed in the text. (b) The actual pulses constituting this sequence. The thin lines represent $\pi/2$ pulses, and the thick lines represent π pulses. The colors of the pulses represent the pulse axes (X or Y), and the direction of them (up or down) represents the two opposite rotation directions (e.g., $+\pi/2$ pulse and $-\pi/2$ pulse). The ellipsis in the plot indicates that the two rows are connected. The plot is a conceptual illustration of the pulse sequence and is not drawn in proportion to the actual time duration. The actual pulse sequence applied in the experiment uses a cosine envelop with π-pulse duration $t_\pi = 40$ ns and pulse spacing $\tau = 10$ ns. (c),(d) Similar plots for the sequence "cXY4-DROID-vXY4-Sym" used for the nanobeam device. The actual pulse sequence applied in experiments uses a Gaussian envelope with π-pulse duration $t_\pi = 30$ ns and pulse spacing $\tau = 30$ ns.

gradient effects [see Fig. 7(e)] from impacting the microwave drive, an additional padding time (10 ns on the nanobeam device and 50 ns on the bulk sample device) per rise or fall edge of the gradient is applied between the gradient pulses and neighboring MW pulses.

J. Hamiltonian engineering

To engineer a desired form of interaction in a spin ensemble, we make use of Floquet engineering techniques described in detail in Ref. [35]. The native form of NV-NV interaction (considering $m_S = -1$, $m_S = 0$ sublevels),

$$H_{\text{int}} = \sum_{ij} J(\boldsymbol{r}_{ij})(S_i^x S_j^x + S_i^y S_j^y - S_i^z S_j^z), \tag{14}$$

is transformed by a sequence of $\pi/2$ and π pulses to a Heisenberg Hamiltonian. By changing pulse spacings, we can continuously tune the form of interaction, as shown in Ref. [35]. In the bulk sample part of this work, we use a new pulse sequence called "cXY8-DROID-vXY4-Mirror" [see Figs. 10(a) and 10(b)], which is an improved version of the "DROID-R2D2" sequence introduced in Ref. [72], with better robustness against coherent pulse errors.

The name of this pulse sequence stands for its structure, which involves the concatenation [73] of the following four pulse sequence layers.

(i) The inner layer is an $XY8$ sequence, targeting at robust disorder decoupling on fastest possible timescale.

(ii) The second layer is the DROID [35] structure that tunes the XXZ anisotropy of the effective Hamiltonian.

(iii) The third layer can be viewed as further concatenation with $XY4$ using virtual pulses [74]. This structure provides improved robustness against coherent pulse errors, as errors accumulated in the first two layers are coherently canceled in this layer. We note that such concatenation with $XY4$ automatically guarantees the satisfaction of all design rules for higher-order dynamical decoupling [72].

(iv) The outer layer is a mirror symmetrization [in terms of the frame representation in Fig. 10(a)] that we found helpful experimentally. We note that previous DROID-type sequences [38,72] also have the same or similar structures.

In this work, the sequence described above results in significant extension of experimental timescales under the SU(2) symmetric Heisenberg Hamiltonian, when compared to DROID-R2D2 [22], as seen in Figs. S1(a) and S1(b) [34].

Similarly, in the nanobeam part of this work, we use another new pulse sequence called "cXY4-DROID-vXY4-Sym," where the inner layer is replaced by an $XY4$ sequence to shorten the total sequence duration and the outer layer is replaced by a slightly different symmetrization. The comparison of experimental timescales to DROID-R2D2 is shown in Figs. S1(c) and S1(d) [34].

K. Numerical simulations of spin dynamics

Numerical simulation of spiral dynamics is done using the discrete truncated Wigner approximation [75], assuming open boundary condition and experimentally motivated sample geometries. Specifically, we simulate $N = 1572$ randomly placed spins for the bulk sample assuming a cylinder geometry of diameter $d = 500$ nm and height $h = 185$ nm and $N = 6750$ spins for the nanobeam with a length double the beam width ($w = 300$ nm). For all numerics, the UV cutoff spatial scale of NV centers is assumed to be 0.2 times the typical spacing (i.e., $r_{\text{UV}} = 6$ nm for the bulk sample and 2.2 nm for the nanobeam).

ACKNOWLEDGMENTS

We are grateful to John Blanchard, Soonwon Choi, Johannes Cremer, Emily J. Davis, Oriana Diessel, Alexander Douglas, Marek Kopciuch, Nazlı Köylüoğlu, Nishad Maskara, Shantam Ravan, Michele Tamagnone, Yaroslav Tserkovnyak, Zilin Wang, Weijie Wu, Norman Yao, Bingtian Ye, and Qian-Ze Zhu for useful discussions. We thank James MacArthur for technical contributions. We also thank Junichi Isoya, Shinobu Onoda, Hitoshi Sumiya, and Fedor Jelezko for providing the black diamond sample. This work was supported in part by the Center for Ultracold Atoms (a National Science Foundation Physics Frontiers Center), the National Science Foundation (Grant No. PHY-2012023), Vannevar Bush Faculty Fellowship Program, U.S. Department of Energy BES Grant No. DE-SC0019241, the Army Research Office through the MURI program Grant No. W911NF-20-1-0136, and Gordon and Betty Moore Foundation Grant No. 7797-01.

N. T. L. conceived the mechanism of collective nonlinearity. P. P. and H. G. performed the experiment with support from L. S. M., O. M., and H. Z. C. S., O. M., and B. M. developed the two-layer gradient device used to control spin dynamics in the black diamond nanobeam. H. G., A. C. M., P. P., and M. M. developed the single-layer gradient device used to control spin dynamics in the bulk diamond sample. L. B. H. W. fabricated the bulk diamond sample. N. T. L. conducted the theoretical analysis with input from H. G., P. P., L. S. M., and M. D. L. S. P., A. C. B. J., F. C., H. P., and M. D. L. supervised all the work. All authors discussed the results and contributed to the manuscript.

There are no competing interests to declare.

DATA AVAILABILITY

The data that support the findings of this article are openly available [76].

[1] Sepehr Ebadi, Tout T. Wang, Harry Levine, Alexander Keesling, Giulia Semeghini, Ahmed Omran, Dolev Bluvstein, Rhine Samajdar, Hannes Pichler, Wen Wei Ho, Soonwon Choi, Subir Sachdev, Markus Greiner, Vladan Vuletić, and Mikhail D. Lukin, *Quantum phases of matter on a 256-atom programmable quantum simulator*, Nature (London) **595**, 227 (2021).

[2] T. I. Andersen, N. Astrakhantsev, A. H. Karamlou *et al.*, *Thermalization and criticality on an analogue–digital quantum simulator*, Nature (London) **638**, 79 (2025).

[3] Tom Manovitz, Sophie H. Li, Sepehr Ebadi, Rhine Samajdar, Alexandra A. Geim, Simon J. Evered, Dolev Bluvstein, Hengyun Zhou, Nazli Ugur Koyluoglu, Johannes Feldmeier, Pavel E. Dolgirev, Nishad Maskara, Marcin Kalinowski, Subir Sachdev, David A. Huse, Markus Greiner, Vladan Vuletić, and Mikhail D. Lukin, *Quantum coarsening and collective dynamics on a programmable simulator*, Nature (London) **638**, 86 (2025).

[4] Soonwon Choi, Joonhee Choi, Renate Landig, Georg Kucsko, Hengyun Zhou, Junichi Isoya, Fedor Jelezko, Shinobu Onoda, Hitoshi Sumiya, Vedika Khemani, Curt Von Keyserlingk, Norman Y. Yao, Eugene Demler, and Mikhail D. Lukin, *Observation of discrete time-crystalline order in a disordered dipolar many-body system*, Nature (London) **543**, 221 (2017).

[5] Guillaume Bornet, Gabriel Emperauger, Cheng Chen, Bingtian Ye, Maxwell Block, Marcus Bintz, Jamie A. Boyd, Daniel Barredo, Tommaso Comparin, Fabio Mezzacapo, Tommaso Roscilde, Thierry Lahaye, Norman Y. Yao, and Antoine Browaeys, *Scalable spin squeezing in a dipolar Rydberg atom array*, Nature (London) **621**, 728 (2023).

[6] Masahiro Kitagawa and Masahito Ueda, *Squeezed spin states*, Phys. Rev. A **47**, 5138 (1993).

[7] Emily Davis, Gregory Bentsen, and Monika Schleier-Smith, *Approaching the Heisenberg limit without single-particle detection*, Phys. Rev. Lett. **116**, 053601 (2016).

[8] D. J. Wineland, J. J. Bollinger, W. M. Itano, and D. J. Heinzen, *Squeezed atomic states and projection noise in spectroscopy*, Phys. Rev. A **50**, 67 (1994).

[9] A. Sørensen, L.-M. Duan, J. I. Cirac, and P. Zoller, *Many-particle entanglement with Bose–Einstein condensates*, Nature (London) **409**, 63 (2001).

[10] C. Gross, T. Zibold, E. Nicklas, J. Estève, and M. K. Oberthaler, *Nonlinear atom interferometer surpasses classical precision limit*, Nature (London) **464**, 1165 (2010).

[11] Max F. Riedel, Pascal Böhi, Yun Li, Theodor W. Hänsch, Alice Sinatra, and Philipp Treutlein, *Atom-chip-based generation of entanglement for quantum metrology*, Nature (London) **464**, 1170 (2010).

[12] Monika H. Schleier-Smith, Ian D. Leroux, and Vladan Vuletić, *Squeezing the collective spin of a dilute atomic ensemble by cavity feedback*, Phys. Rev. A **81**, 021804(R) (2010).

[13] Onur Hosten, Nils J. Engelsen, Rajiv Krishnakumar, and Mark A. Kasevich, *Measurement noise 100 times lower than the quantum-projection limit using entangled atoms*, Nature (London) **529**, 505 (2016).

[14] Simone Colombo, Edwin Pedrozo-Peñafiel, Albert F. Adiyatullin, Zeyang Li, Enrique Mendez, Chi Shu, and Vladan Vuletić, *Time-reversal-based quantum metrology with many-body entangled states*, Nat. Phys. **18**, 925 (2022).

[15] Zeyang Li, Simone Colombo, Chi Shu, Gustavo Velez, Saúl Pilatowsky-Cameo, Roman Schmied, Soonwon Choi, Mikhail Lukin, Edwin Pedrozo-Peñafiel, and Vladan Vuletić, *Improving metrology with quantum scrambling*, Science **380**, 1381 (2023).

[16] Justin G. Bohnet, Brian C. Sawyer, Joseph W. Britton, Michael L. Wall, Ana Maria Rey, Michael Foss-Feig, and John J. Bollinger, *Quantum spin dynamics and entanglement generation with hundreds of trapped ions*, Science **352**, 1297 (2016).

[17] Johannes Franke, Sean R. Muleady, Raphael Kaubruegger, Florian Kranzl, Rainer Blatt, Ana Maria Rey, Manoj K. Joshi, and Christian F. Roos, *Quantum-enhanced sensing on optical transitions through finite-range interactions*, Nature (London) **621**, 740 (2023).

[18] Jun-Ru Li, Kyle Matsuda, Calder Miller, Annette N. Carroll, William G. Tobias, Jacob S. Higgins, and Jun Ye, *Tunable itinerant spin dynamics with polar molecules*, Nature (London) **614**, 70 (2023).

[19] Calder Miller, Annette N. Carroll, Junyu Lin, Henrik Hirzler, Haoyang Gao, Hengyun Zhou, Mikhail D. Lukin, and Jun Ye, *Two-axis twisting using Floquet-engineered XYZ spin models with polar molecules*, Nature (London) **633**, 332 (2024).

[20] Alec Douglas, Vassilios Kaxiras, Lin Su, Michal Szurek, Vikram Singh, Ognjen Marković, and Markus Greiner, *Spin squeezing with itinerant magnetic dipoles*, Phys. Rev. X **15**, 041021 (2025).

[21] Nabeel Aslam, Hengyun Zhou, Elana K. Urbach, Matthew J. Turner, Ronald L. Walsworth, Mikhail D. Lukin, and Hongkun Park, *Quantum sensors for biomedical applications*, Nat. Rev. Phys. **5**, 157 (2023).

[22] Hengyun Zhou, Leigh S. Martin, Matthew Tyler, Oksana Makarova, Nathaniel Leitao, Hongkun Park, and Mikhail D. Lukin, *Robust higher-order hamiltonian engineering for quantum sensing with strongly interacting systems*, Phys. Rev. Lett. **131**, 220803 (2023).

[23] Nithya Arunkumar, Kevin S. Olsson, Jner Tzern Oon, Connor A. Hart, Dominik B. Bucher, David R. Glenn, Mikhail D. Lukin, Hongkun Park, Donhee Ham, and Ronald L. Walsworth, *Quantum logic enhanced sensing in solid-state spin ensembles*, Phys. Rev. Lett. **131**, 100801 (2023).

[24] K. Arai, C. Belthangady, H. Zhang, N. Bar-Gill, S. J. DeVience, P. Cappellaro, A. Yacoby, and R. L. Walsworth, *Fourier magnetic imaging with nanoscale resolution and compressed sensing speed-up using electronic spins in diamond*, Nat. Nanotechnol. **10**, 859 (2015).

[25] M. S. Grinolds, M. Warner, K. De Greve, Y. Dovzhenko, L. Thiel, R. L. Walsworth, S. Hong, P. Maletinsky, and A. Yacoby, *Subnanometre resolution in three-dimensional*

magnetic resonance imaging of individual dark spins, Nat. Nanotechnol. **9**, 279 (2014).

[26] Haoyang Gao, Leigh S. Martin, Lillian B. Hughes, Nathaniel T. Leitao, Piotr Put, Hengyun Zhou, Nazli U. Koyluoglu, Simon A. Meynell, Ania C. Bleszynski Jayich, Hongkun Park, and Mikhail D. Lukin, *Signal amplification in a solid-state sensor through asymmetric many-body echo*, Nature (London) **646**, 68 (2025).

[27] Weijie Wu, Emily J. Davis, Lillian B. Hughes, Bingtian Ye, Zilin Wang, Dominik Kufel, Tasuku Ono, Simon A. Meynell, Maxwell Block, Che Liu, Haopu Yang, Ania C. Bleszynski Jayich, and Norman Y. Yao, *Spin squeezing in an ensemble of nitrogen–vacancy centres in diamond*, Nature (London) **646**, 74 (2025).

[28] M. P. Kwasigroch and N. R. Cooper, *Synchronization transition in dipole-coupled two-level systems with positional disorder*, Phys. Rev. A **96**, 053610 (2017).

[29] Hengyun Zhou, Joonhee Choi, Soonwon Choi, Renate Landig, Alexander M. Douglas, Junichi Isoya, Fedor Jelezko, Shinobu Onoda, Hitoshi Sumiya, Paola Cappellaro, Helena S. Knowles, Hongkun Park, and Mikhail D. Lukin, *Quantum metrology with strongly interacting spin systems*, Phys. Rev. X **10**, 031003 (2020).

[30] Marcus W. Doherty, Neil B. Manson, Paul Delaney, Fedor Jelezko, Jörg Wrachtrup, and Lloyd C. L. Hollenberg, *The nitrogen-vacancy colour centre in diamond*, Phys. Rep. **528**, 1 (2013).

[31] G. Kucsko, S. Choi, J. Choi, P. C. Maurer, H. Zhou, R. Landig, H. Sumiya, S. Onoda, J. Isoya, F. Jelezko, E. Demler, N. Y. Yao, and M. D. Lukin, *Critical thermalization of a disordered dipolar spin system in diamond*, Phys. Rev. Lett. **121**, 023601 (2018).

[32] Francesco Casola, Toeno Van Der Sar, and Amir Yacoby, *Probing condensed matter physics with magnetometry based on nitrogen-vacancy centres in diamond*, Nat. Rev. Mater. **3**, 17088 (2018).

[33] Paul Niklas Jepsen, Yoo Kyung Eunice Lee, Hanzhen Lin, Ivana Dimitrova, Yair Margalit, Wen Wei Ho, and Wolfgang Ketterle, *Long-lived phantom helix states in Heisenberg quantum magnets*, Nat. Phys. **18**, 899 (2022).

[34] See Supplemental Material at http://link.aps.org/supplemental/10.1103/hyrk-1ftz for experimental details and theoretical derivations.

[35] Leigh S. Martin, Hengyun Zhou, Nathaniel T. Leitao, Nishad Maskara, Oksana Makarova, Haoyang Gao, Qian-Ze Zhu, Mincheol Park, Matthew Tyler, Hongkun Park, Soonwon Choi, and Mikhail D. Lukin, *Controlling local thermalization dynamics in a Floquet-engineered dipolar ensemble*, Phys. Rev. Lett. **130**, 210403 (2023).

[36] Nathaniel T. Leitao, Leigh S. Martin, Haoyang Gao, Piotr Put, and Mikhail D. Lukin, *Scalable spin squeezing from critical spin hydrodynamics* (to be published).

[37] J. S. Waugh, L. M. Huber, and U. Haeberlen, *Approach to high-resolution NMR in solids*, Phys. Rev. Lett. **20**, 180 (1968).

[38] Joonhee Choi, Hengyun Zhou, Helena S. Knowles, Renate Landig, Soonwon Choi, and Mikhail D. Lukin, *Robust dynamic Hamiltonian engineering of many-body spin systems*, Phys. Rev. X **10**, 031002 (2020).

[39] Joonhee Choi, Soonwon Choi, Georg Kucsko, Peter C. Maurer, Brendan J. Shields, Hitoshi Sumiya, Shinobu Onoda, Junichi Isoya, Eugene Demler, Fedor Jelezko, Norman Y. Yao, and Mikhail D. Lukin, *Depolarization dynamics in a strongly interacting solid-state spin ensemble*, Phys. Rev. Lett. **118**, 093601 (2017).

[40] N. D. Mermin and H. Wagner, *Absence of ferromagnetism or antiferromagnetism in one- or two-dimensional isotropic Heisenberg models*, Phys. Rev. Lett. **17**, 1133 (1966).

[41] Robert V. Lange, *Interaction range, the Goldstone theorem, and long-range order in the Heisenberg ferromagnet*, Phys. Rev. **156**, 630 (1967).

[42] Bertrand I. Halperin, *On the Hohenberg–Mermin–Wagner theorem and its limitations*, J. Stat. Phys. **175**, 521 (2019).

[43] John David Jackson, *Classical Electrodynamics* (John Wiley & Sons, New York, 2012).

[44] Žiga Krajnik, Enej Ilievski, and Tomaž Prosen, *Undular diffusion in nonlinear sigma models*, Phys. Rev. Lett. **125**, 240607 (2020).

[45] Paolo Glorioso, Luca Delacrétaz, Xiao Chen, Rahul Nandkishore, and Andrew Lucas, *Hydrodynamics in lattice models with continuous non-Abelian symmetries*, SciPost Phys. **10**, 015 (2021).

[46] Edward B. Fel'dman and Serge Lacelle, *Configurational averaging of dipolar interactions in magnetically diluted spin networks*, J. Chem. Phys. **104**, 2000 (1996).

[47] Michael Foss-Feig, Zhe-Xuan Gong, Alexey V. Gorshkov, and Charles W. Clark, *Entanglement and spin-squeezing without infinite-range interactions*, arXiv:1612.07805.

[48] Warren S. Warren, Wolfgang Richter, Amy Hamilton Andreotti, and Bennett T. Farmer, *Generation of impossible cross-peaks between bulk water and biomolecules in solution NMR*, Science **262**, 2005 (1993).

[49] M. V. Romalis and M. P. Ledbetter, *Transverse spin relaxation in liquid X 129 e in the presence of large dipolar fields*, Phys. Rev. Lett. **87**, 067601 (2001).

[50] M. P. Ledbetter and M. V. Romalis, *Nonlinear effects from dipolar interactions in hyperpolarized liquid X 129 e*, Phys. Rev. Lett. **89**, 287601 (2002).

[51] Sarang Gopalakrishnan and Romain Vasseur, *Kinetic theory of spin diffusion and superdiffusion in XXZ spin chains*, Phys. Rev. Lett. **122**, 127202 (2019).

[52] B. Ye, F. Machado, C. D. White, Roger S. K. Mong, and N. Y. Yao, *Emergent hydrodynamics in nonequilibrium quantum systems*, Phys. Rev. Lett. **125**, 030601 (2020).

[53] C. Zu, F. Machado, B. Ye, S. Choi, B. Kobrin, T. Mittiga, S. Hsieh, P. Bhattacharyya, M. Markham, D. Twitchen, A. Jarmola, D. Budker, C. R. Laumann, J. E. Moore, and N. Y. Yao, *Emergent hydrodynamics in a strongly interacting dipolar spin ensemble*, Nature (London) **597**, 45 (2021).

[54] Lyndon Emsley, *Spin diffusion for NMR crystallography*, in *eMagRes*, 10.1002/9780470034590.emrstm1010 (2009).

[55] Ekaterina Dikarov, Oleg Zgadzai, Yaron Artzi, and Aharon Blank, *Direct measurement of the flip-flop rate of electron spins in the solid state*, Phys. Rev. Appl. **6**, 044001 (2016).

[56] Laurent P. Lévy and Andrei E. Ruckenstein, *Collective spin oscillations in spin-polarized gases: Spin-polarized hydrogen*, Phys. Rev. Lett. **52**, 1512 (1984).

[57] Paul Niklas Jepsen, Jesse Amato-Grill, Ivana Dimitrova, Wen Wei Ho, Eugene Demler, and Wolfgang Ketterle, *Spin*

transport in a tunable Heisenberg model realized with ultracold atoms, Nature (London) **588**, 403 (2020).

[58] Paul Niklas Jepsen, Wen Wei Ho, Jesse Amato-Grill, Ivana Dimitrova, Eugene Demler, and Wolfgang Ketterle, *Transverse spin dynamics in the anisotropic Heisenberg model realized with ultracold atoms*, Phys. Rev. X **11**, 041054 (2021).

[59] Sebastian Hild, Takeshi Fukuhara, Peter Schauß, Johannes Zeiher, Michael Knap, Eugene Demler, Immanuel Bloch, and Christian Gross, *Far-from-equilibrium spin transport in Heisenberg quantum magnets*, Phys. Rev. Lett. **113**, 147205 (2014).

[60] B. A. Bernevig, J. Orenstein, and S.-C. Zhang, *Exact SU(2) symmetry and persistent spin helix in a spin-orbit coupled system*, Phys. Rev. Lett. **97**, 236601 (2006).

[61] J. D. Koralek, C. P. Weber, J. Orenstein, B. A. Bernevig, Shou-Cheng Zhang, S. Mack, and D. D. Awschalom, *Emergence of the persistent spin helix in semiconductor quantum wells*, Nature (London) **458**, 610 (2009).

[62] Juan A. Acebrón, L. L. Bonilla, Conrad J. Pérez Vicente, Félix Ritort, and Renato Spigler, *The Kuramoto model: A simple paradigm for synchronization phenomena*, Rev. Mod. Phys. **77**, 137 (2005).

[63] Peter Reimann, Patrick Vorndamme, and Jürgen Schnack, *Nonequilibration, synchronization, and time crystals in isotropic Heisenberg models*, Phys. Rev. Res. **5**, 043040 (2023).

[64] Marko Medenjak, Berislav Buča, and Dieter Jaksch, *Isolated Heisenberg magnet as a quantum time crystal*, Phys. Rev. B **102**, 041117(R) (2020).

[65] H. Gao, N. T. Leitao, S. Dandavate, Lillian B. Hughes Wyatt, P. Put, M. Mammen, L. S. Martin, H. Park, Ania C. Bleszynski Jayich, and M. D. Lukin, *Dressed-state Hamiltonian engineering in a strongly interacting solid-state spin ensemble*, Phys. Rev. Lett. **136**, 200802 (2026).

[66] Nathaniel T. Leitao, Haoyang Gao, Leigh S. Martin, and Mikhail D. Lukin, *Optimally scalable, robust signal amplification via asymmetric time-reversal of collective many-body physics* (to be published).

[67] Haoyang Gao, Piotr Put, Nathaniel T. Leitao *et al.*, *Nanoscale magnetometry via collective many-body dynamics in diamond*, arXiv:2609.03039.

[68] R. Budakian *et al.*, *Roadmap on nanoscale magnetic resonance imaging*, Nanotechnology **35**, 412001 (2024).

[69] Zhongzhi Guo, You Huang, Mingcheng Cai, Chunxing Li, Mengze Shen, Mengqi Wang, Pei Yu, Ya Wang, Fazhan Shi, Pengfei Wang, and Jiangfeng Du, *Wide-field Fourier magnetic imaging with electron spins in diamond*, npj Quantum Inf. **10**, 24 (2024).

[70] Mohammad T. Amawi, Andrii Trelin, You Huang, Paul Weinbrenner, Francesco Poggiali, Joachim Leibold, Martin Schalk, and Friedemann Reinhard, *Three-dimensional magnetic resonance tomography with sub-10 nanometer resolution*, npj Quantum Inf. **10**, 16 (2024).

[71] Nazlı Uğur Köylüoğlu, Nathaniel T. Leitao, Leigh S. Martin, Haoyang Gao, Piotr Put, and Mikhail D. Lukin, *Interaction-enhanced many-body covariance magnetometry for strongly interacting quantum sensors* (to be published).

[72] Matthew Tyler, Hengyun Zhou, Leigh S. Martin, Nathaniel Leitao, and Mikhail D. Lukin, *Higher-order methods for Hamiltonian engineering pulse sequence design*, Phys. Rev. A **108**, 062602 (2023).

[73] K. Khodjasteh and D. A. Lidar, *Fault-tolerant quantum dynamical decoupling*, Phys. Rev. Lett. **95**, 180501 (2005).

[74] Gonzalo A. Álvarez, Alexandre M. Souza, and Dieter Suter, *Iterative rotation scheme for robust dynamical decoupling*, Phys. Rev. A **85**, 052324 (2012).

[75] J. Schachenmayer, A. Pikovski, and A. M. Rey, *Many-body quantum spin dynamics with Monte Carlo trajectories on a discrete phase space*, Phys. Rev. X **5**, 011022 (2015).

[76] Piotr Put, Nathaniel Leitao, Haoyang Gao, Christina Spägele, Oksana Makarova, Lillian Hughes, Andrew Maccabe, Mathew Mammen, Bartholomeus Machielse, Hengyun Zhou, Szymon Pustelny, Ania Jayich, Federico Capasso, Leigh Martin, Hongkun Park, and Mikhail Lukin, *Collective many-body dynamics in a solid-state quantum sensor controlled through nanoscale magnetic gradients*, https://zenodo.org/records/22080698 (2026).